



Research Paper

Optical coherence tomographic measurements of the sound-induced motion of the ossicular chain in chinchillas: Additional modes of ossicular motion enhance the mechanical response of the chinchilla middle ear at higher frequencies

John J. Rosowski^{a,b,*}, Antoine Ramier^{c,d}, Jeffrey Tao Cheng^{a,b}, Seok-Hyun Yun^{c,d}

^a Eaton-Peabody Laboratory of Auditory Physiology, Massachusetts Eye and Ear, 243 Charles Street, Boston 02114, MA, USA

^b Department of Otolaryngology – Head and Neck Surgery, Harvard Medical School, 243 Charles Street, Boston 02114, MA, USA

^c Harvard-MIT Division of Health Sciences and Technology, 77 Massachusetts Avenue, Cambridge 02139 MA, USA

^d Wellman Center for Photomedicine, Massachusetts General Hospital, 65 Lansdowne St. UP-5, Cambridge 02139, MA, USA

ARTICLE INFO

Article history:

Received 15 April 2020

Revised 18 July 2020

Accepted 6 August 2020

Available online 12 August 2020

Keywords:

Ossicular function

Middle ear

Modes of ossicular motion

ABSTRACT

Wavelength-swept optical coherence tomography (OCT) was used to scan the structure of cadaveric chinchilla ears in three dimensions with high spatial resolution and measure the sound-induced displacements of the entire OCT-visible lateral surfaces of the ossicles in the lateral-to-medial direction. The simultaneous measurement of structure and displacement allowed a precise match between the observed motion and its structural origin. The structure and measured displacements are consistent with previously published data. The coincident detailed structural and motion measurements demonstrate the presence of several frequency-dependent modes of ossicular motion, including: (i) rotation about an anteriorly-to-posteriorly directed axis positioned near the commonly defined anatomical axis of rotation that dominates at frequencies below 8 kHz, (ii) a lateral-to-medial translational component that is visible at frequencies from 2 to greater than 10 kHz, and (iii) a newly described rotational mode around an inferiorly-to-superiorly directed axis that parallels the manubrium of the malleus and dominates ossicular motion between 10 and 16 kHz. This new axis of rotation is located near the posterior edge of the manubrium. The onset of the second rotational mode leads to a boost in the magnitude of sound-induced stapes displacement near 14 kHz, and adds a half-cycle to the accumulating phase in middle-ear sound transmission. Similar measurements in one ear after interruption of the incudostapedial joint suggest the load of the cochlea and stapes annular ligament is important to the presence of the second rotational mode, and acts to limit simple ossicular translation.

© 2020 Elsevier B.V. All rights reserved.

1. Introduction

The middle ear – which includes the tympanic membrane (TM), the ossicles, their suspensory ligaments, connecting joints, controlling muscles and the middle-ear air spaces – couples sound pressure in the ear canal near the TM P_{EC} to the sound pressure in the vestibule of the inner ear P_V . This coupling depends on the sound-induced stapes displacement X_S (Peake et al. 1992) that evokes P_V . Measurements of the frequency-dependent transfer of sound through the middle ear (in terms of either $P_V(f)/P_{EC}(f)$

or $X_S(f)/P_{EC}(f)$ ¹) in multiple mammalian species describe continued high-level output at stimulus frequencies well above the middle-ear resonance frequency, and a phase angle relative to the sound stimulus ($\angle P_V(f)/P_{EC}(f) = \angle P_V(f) - \angle P_{EC}(f)$) that accumulates multiple cycles of phase delay as frequency increases above 10 kHz (Guinan and Peake 1967; Olson 1998; Ruggero and Temchin 2002; Nakajima et al. 2009; Dong et al. 2013; Ravicz and Rosowski 2013; Robles et al. 2015)². The mechanisms responsible for such behavior are not well understood. Table 1 lists the variable names and technical and anatomical terms used throughout the text.

* Corresponding author at: Eaton-Peabody Laboratory, Massachusetts Eye and Ear Infirmary, 243 Charles Street, Boston 02114, MA, USA.

E-mail address: john_rosowski@meei.harvard.edu (J.J. Rosowski).

¹ These mechano-acoustic variables and transfer functions are quantified in the sinusoidal steady state whereby $(t) = |Y(f)| \cos(2\pi ft + \angle Y(f))$, and $Y(f) = |Y(f)| e^{i2\pi \angle Y(f)}$.

² In the rest of this article, the mechano-acoustic variables are implicit functions of frequency.

Table 1

<i>Anatomical abbreviations</i>	
aml	– the anterior-malleal ligament described by Vrettakos et al. (1988)
ISJ	– the incudostapedial joint
TM	– the tympanic membrane
AP axis	– the anterior-posterior ossicular axis
IS axis	– the inferior-superior ossicular axis
<i>Technique relevant abbreviations and nomenclature</i>	
A-Line	– the line of single wavelength-swept OCT laser signal
B-Scan	– a one-dimensional scan of A-lines that defines the reflectance and sound-induced motion in a two-dimensional plane.
FFT	– Fast Fourier Transform that defines the magnitude and phase of optical reflectance along the recorded A-line.
OCT	– Optical Coherence Tomography
ROI	– Regions of Interest regions of the reconstructed anatomy that contain moving ossicles.
X	– the complex number describing the magnitude and phase of a sound-induced displacement.
X	– the magnitude of the complex number describing displacement at one frequency.
$\angle X$	– the phase angle of the complex number describing displacement at one frequency.
<i>Measured variables</i>	
f	– frequency
P_{EC}	– The complex sound pressure measured in the ear canal remnant near the lateral surface of the TM.
P_V	– The complex sound pressure in the vestibule of the inner ear.
P_{EC}/P_V	– The complex sound pressure gain produced by the middle ear.
X_S	– The complex sound-induced displacement of the stapes.

Several authors have noted similarities between the frequency-dependence of sound transfer through the middle ear and that of a ‘matched’ transmission line (Decraemer et al. 1997; Olson 1998; Puria and Allen 1998). Puria and Allen (1998) described how the mechanical masses and stiffnesses distributed through the ossicular system approximate a transmission line that when perfectly matched to the impedance of the inner ear load can provide a frequency-independent magnitude of sound pressure gain ($|P_V/P_{EC}|$) and a frequency-dependent sound transfer phase angle (either $\angle P_V/P_{EC}$ or $\angle X_S/P_{EC}$) consistent with a simple delay. The matched transmission-line prediction of high-level magnitude responses and multiple cycles of accumulated phase delay in response to high-frequency sound stimuli is different from simpler lumped models of middle-ear function that predict high-frequency middle-ear function is dominated by the resistance of the cochlea and the masses of the ossicles and the entrained cochlear fluid (Zwislocki 1962; Møller 1963; Kringlebotn 1988; Hemilä et al. 1995).

Both transmission line and lumped models often describe only one mode of ossicular motion that produce one-dimensional in-and-out motions of the stapes. These contrast with finite-element models of the middle ear and TM that allow for complex three-dimensional motions within the middle ear (Ladak and Funnell 1996; Blayney et al. 1997; Koike et al. 2002; Gan et al. 2004; O’Connor et al. 2017; Wang and Gan 2016). In between these two cases are lumped-element multi-dimensional multi-modal models of ossicular motion, such as those proposed by Fleischer (1978), Hudde and Weistenhöfer (1997), and Puria and Steele (2010).

The simplest of these models is that of Fleischer (1978), who used mechanical models of rigid ossicles rotating about fixed axes, and suggested the ossicular systems of different mammals rotate about more than one axis, depending on the frequency of the sound stimulus. Fleischer (1978) argued that the commonly cited (e.g. Dahmann 1929; Békésy 1960; Kirikae 1960) anterior-posterior³ axis (AP axis) of rotation of the malleus and incus (Fig. 1a) – anchored by the anterior-process of the malleus on one end and the posterior-incudal ligament on the other – is a prominent feature in mammalian auditory function when the stimulus frequency is near or below the ear’s first resonance frequency. In ears that appear specialized for low-frequency (<3 kHz) hearing (as defined by Fleischer (1978) to include humans, other pri-

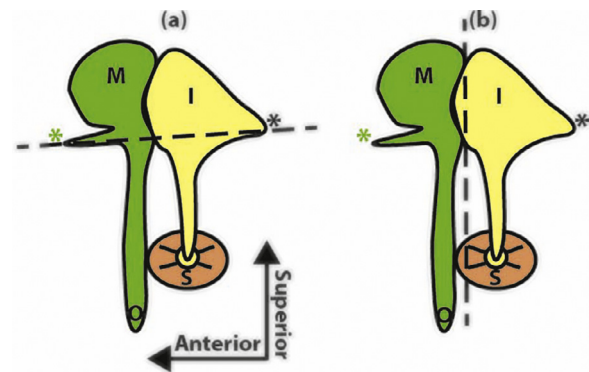


Fig. 1. The rotation of the ossicles in two mammal ears. Axes of ossicular rotation (the dashed black lines) as defined by Fleischer (1978) or Puria and Steele (2010): (a) freely-mobile ear with Fleischer’s low-frequency axis of rotation; (b) freely-mobile ear with the high-frequency axis of rotation predicted by Puria and Steele (2010). The mallei (M) are colored green. The inci (I) are colored yellow. The stapes footplates (S) are colored orange. Green *’s mark the tips of the anterior process of the malleus. Black *’s mark the location of the posterior-incudal ligament. The o’s mark the umbo, the center of the spoon-like region centered within the inferior tip of the manubrium (the handle) of the malleus. The illustrated ossicles are from the left side of the head. (For interpretation of the references to color in this figure legend, the reader is referred to the web version of this article.)

mates, chinchillas, guinea pigs and others with highly compliant ‘freely mobile’ ossicular systems) the handle of the malleus (or manubrium) and the inferior or distal process of the incus (the long process in humans) are both perpendicular to the AP axis of rotation, and are located inferior to this axis (Fig. 1a). Rotations about the AP axis cause both the umbo (the central depression in the spoon-like tip of the manubrium) and the inferior incus with the attached stapes to move laterally and medially in-phase (in and out together). There is significant experimental support for such low-frequency rotation in multiple mammalian ears (e.g. Dahmann 1929; Wever and Lawrence 1954; Kirikae 1960; Guinan and Peake 1967; Manley and Johnstone 1974; Ruggiero et al. 1990; Decraemer et al. 1991; Decraemer and Khanna 1994; Rosowski et al. 1999; Decraemer et al. 2014).

An example of a second axis of rotation has been suggested by Puria and Steele (2010) based on mechanical analyses of the isolated malleus, incus and stapes (ignoring the connecting and supporting ligaments) of four mammalian species (human, chinchilla, guinea pig and cat). In all of these mammals the malleus and incus begin as separate structures during development. During the life

³ Throughout this paper we adapt the human oriented positional anatomic descriptors, where dorsal is superior, ventral is inferior, rostral is anterior and caudal is posterior.

spans of human and cat, the incus and malleus remain separate bony structures connected by the incudomalleolar joint; however, in chinchilla and guinea pig the malleus and incus are conjoined by bone in the adult ear. The Puria and Steele analysis suggested this difference in ossicular connection leads to fundamental differences in ossicular function, as the separate bony malleus and incus in human and cat permits the development of an additional mode of ossicular rotation at higher frequencies about an axis perpendicular to that of Fig. 1a and centered within the incudomalleolar joint as in Fig. 1b.

This additional motion mode was hypothesized to (a) produce out-of-phase motion of the incus and malleus, and (b) extend the high-frequency range of incus and stapes motion by providing a mode of ossicular motion with a higher stiffness, higher moment of inertia and a corresponding higher resonant frequency. This argument for the benefit of additional rotational modes during high-frequency ossicular motion is nearly identical to that of Fleischer (1978). Puria and Steele also argued that the 'high-frequency boost' introduced by the additional motion mode did not occur in adult chinchilla or guinea pig where the malleus and incus are conjoined. Contrary to this suggestion, the results of new ossicular motion measurements in intact cadaveric chinchilla ears presented in this paper identify a similar, but fundamentally different, mode of ossicular motion in chinchilla and support the notion that frequency-dependent changes in the mode of motion can increase ossicular sound transmission in specific frequency ranges.

The new motion measurements we report were gathered using optical coherence tomography (OCT). OCT is a light-based (usually in the near-infrared region) measurement system that uses interference between a reference light and light reflected from objects to define the density of objects (via the magnitude of the reflected light) and relative distance to objects (via optical group delay). The spatial resolution (5 to 30 μm) and penetration of OCT (better than 3 mm in soft tissues) is sufficiently high to image normal and pathologic middle-ear structures behind the TM (Pitris et al. 2001; Djalilian et al. 2010; Subhash et al. 2012; Chang et al. 2013; Burkhardt et al. 2014; Park et al. 2014, 2016; MacDougall et al. 2016; Ramier et al. 2018a). OCT can also measure the motion of the identified structures (via temporal changes in the interference phase) with noise floors of about 10 nm (MacDougall et al. 2016; Ramier et al. 2018b). OCT's co-determination of structure and motion eliminates the influence of the motion of nearby structures on motion measurements, which has been a problem in other laser-based motion measurements (e.g. de La Rochefoucauld et al. 2005).

2. Methods

2.1. The OCT and control systems

The combined stimulus, imaging and data acquisition system has been described in Ramier et al. (2018a). Briefly, a rotating polygon mirror was used to produce a wavelength-swept laser beam with a center wavelength of 1280 nm with an 80 nm 3 dB bandwidth at a repetition rate of 45 kHz. A fiber-based Mach-Zehnder interferometer splits the laser beam into a sample arm and a reference arm. The sample-arm light was scanned in the two dimensions orthogonal to the beam by a pair of galvanometer-controlled mirrors. The scanned beam was focused to a spot size of 30 μm . The temporally varying light intensity resulting from the interference of the reference- and sample-arm light was digitized by a balanced photodiode. A computer-controlled multi-channel input/output board (i) generated stimulus waveforms to drive the earphone, (ii) generated DC voltages to control the galvanometers, and (iii) measured the time-locked acoustic stimulus and the response of the photodiode during each laser wavelength sweep. As

a result, each sweep of the laser wavelength (with a period of 1/45000 s) produced an axial 'A-line' interference image from a single galvanometer-determined location, where each A-line was time-locked with the stimulus generator and acoustic measurement systems.

The two galvanometer-controlled mirrors that steered the OCT beam essentially altered the direction of the beam by a small range of angles. The center of the galvanometers was on the order of 250 mm from the TM surface and the beam spread over the scanned 6 mm \times 6 mm measurement area was well approximated by a uniform plane wave. The galvanometers scanned the sample with 128 equally-spaced A-lines along the x -axis (anterior to posterior) and the y -axis (superior to inferior) with a line density of $\sim 47 \mu\text{m}$ in each dimension (128 points per 6 mm) or $\sim 0.002 \text{ mm}^2$ in two dimensions (128 by 128 points over $\sim 36 \text{ mm}^2$).

2.2. Image-intensity maps and scaling

The optical intensity measured during each A-line sweep describes a wavelength domain interferogram, which was corrected for background noise, filtered and then Fourier transformed to produce a complex function in z , where each Fourier line is ordinarily associated with a specific z value (the spacing of the Fourier lines determined the spatial resolution in the z direction). The magnitude of this complex function in z represents the optical intensity of the reflections from structures along the z -axis. The duration and wavelength variations within each laser sweep resulted in a theoretical penetration depth of 8 mm with a 7.8 μm axial resolution (8 mm/1024 spectral lines). In practice the penetration depth was limited to 3 to 4 mm by the dense petrous bone medial to the middle-ear structures.

Sweeping the A-lines in the posterior to anterior (x) direction with the superior to inferior (y) dimension held constant produced two dimensional 'B-scans', e.g. Fig. 2. Each B-scan is an iso- y section through a three-dimensional rectangular solid, where the 4 corners of the scans are aligned in the x (posterior to anterior) and z (lateral to medial) dimensions. Stacking B-scans at varied y produced volume reconstructions (Fig. 3) of the interference intensity and phase produced by the sample with a resolution of 47 μm in x by 47 μm in y by 7.8 μm in z resulting in a voxel volume of about $1.7 \times 10^4 \mu\text{m}^3$ (or $1.7 \times 10^{-5} \text{ mm}^3$). To improve contrast and enable clearer visualization in the B-scans and three-dimensional reconstructions, the optical intensity of each voxel, defined by the Fourier magnitude of the A-line data, was transformed to a dB scale before conversion to the gray-scaled images used for visualization (Figs. 2 and 3). Amira® software was used to process the three-dimensional reconstructions of the scaled and stacked B-scans. In each reconstruction manual thresholding reduced the visibility of voxels with low-intensity to best visualize the most reflective structures.

2.3. Vibrometry

As described above, the μm scale position in z of each reflecting object was coded by the order of the Fourier components of the time-varying interference intensity produced by each A-line. While the magnitude of each Fourier component defined the optical reflectance of the structures located at each z position, the phase of each component defined the z -axis location of the reflecting object with sub-wavelength accuracy. Differences in this phase between two temporally separated measurements defined a motion of the reflecting object. During sound stimulation, 200 repeated A-lines were taken at each x - y location, and the temporal variations in the phase of the complex intensity at each location were used to describe the displacement as a function of time. The

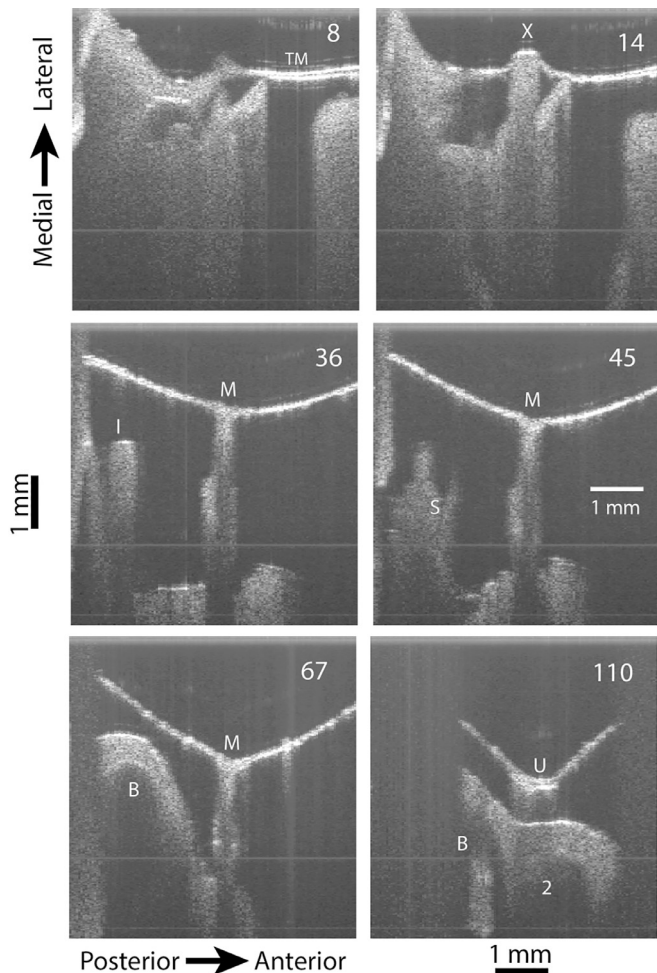


Fig. 2. Six 'B-scans' of the TM and ossicles of the right ear of CH2 taken at different y (superior-inferior) positions. In each B-scan, z (the lateral-medial direction) varies from top-to-bottom and x (the posterior-anterior direction) varies from left to right. The range of x and z coordinates of each scan are identical. B-scan #8 illustrates the measured OCT reflection from a posterior to anterior scan near the superior most region of the TM, and describes a small posterior-anterior TM section (TM), while the rest of the scan illustrates the bone that supports the TM. B-scan #14 is a little more inferior and describes the thin TM on either side of the lateral process of the malleus (X). B-scan #36 is positioned more inferiorly and describes the TM on either side of the manubrium of the malleus (M, differentiated by its thickness and the shadow it casts in z) and the lateral surface and shadow of the inferior tip of the incus (I). B-scan #45 describes the TM on either side of the manubrium of the malleus (M, differentiated by the shadow it casts in z) and the lateral surface and shadow of the stapes head and anterior crus (S). B-scan #67 describes the TM on either side of the manubrium of the malleus and the lateral and medial surface of the petrous bone that covers the base of the chinchilla cochlea (B). B-scan #110 describes the TM on either side of the umbo (U) of the malleus and the lateral surface of the petrous bone that covers the basal (B) and middle (2) turns of the chinchilla cochlea. The inferior to superior distances relative to the lateral process of the malleus of the 6 different B-scans are: -0.28 mm for scan 8, 0 mm for scan 14, 1.03 mm for scan 36, 1.46 mm for scan 45, 2.5 mm for scan 67 and 4.5 mm for scan 110. The identical arrangement of the sections in x and z allows observation of the concavity of the TM, e.g. B-scan #4 shows the z position of the lateral process to be about 0.4 mm from the upper edge of the image, while B-scan #100 shows the umbo to be about 1.5 mm more lateral.

displacement vs. time function at each location was Fourier transformed to define the magnitude and phase of displacement. The ability to discriminate different phases of the interference intensity waveform at each x - y - z location (or voxel) defined the resolution of our displacement measurements. This resolution depended on the number of A-lines used to define the displacement vs. time function and the intensity of the reflected light within each voxel (if the intensity was too small, the recorded time waveform was

noisy). Functional displacement resolution in this study was better than 10 – 20 nm (Ramier et al. 2018a&b).

2.4. Lateral surface definition and displacement averaging

Three-dimensional maps (in x , y and z) of the lateral-most surfaces of the TM and ossicles (e.g. Supplemental Materials 4 through 8) were defined within selected regions of interest (ROIs) in each of the 128 B-scans (e.g. Fig. 2). The ROIs were rectangles drawn around the identified manubrium, incus, stapes anterior crus and footplate. The lateral surfaces within the ROIs were identified by locating the lateral-most z values where a low to high step increase in the dB scaled image intensity occurred. The threshold-intensity step size was adjusted to provide a good match between the computer-detected edges and the visually perceived lateral most edges of the ossicles in each B-scan. The three-dimensional coordinates of the identified lateral surfaces of the manubrium, incus, anterior crus and stapes footplate were stored for later image segmentation, and investigations of the relationship between ossicular geometry and the sound-induced motion.

Two-dimensional maps of ossicular displacement (e.g., Figs. 6–8) were constructed based on the x and y coordinates of the identified ossicular surfaces. The computed sound-induced displacement at each point on the identified ossicular surface was the average of the complex displacement in the 10 voxels with the same x and y coordinates just medial to the surface boundary. Only voxels with a significant image intensity and computed motion magnitude greater than 15 nm were included in the average.

The sound-induced displacement of 8 specific locations on the surface of the ossicles (see Fig. 5A) were defined by averaging the complex motions within a square of 25 voxels (in x and y) centered at each of the 8 locations on the two-dimensional maps. The local averaged motion was determined at: the umbo, a mid-manubrium position (centered on the manubrium at a y -position half way up the manubrium), the lateral process of the manubrium (the rounded bump on the manubrium just below the most superior location of the manubrium), a $\frac{1}{4}$ manubrium position half-way between the umbo and the mid-manubrium, a $\frac{3}{4}$ manubrium position half way between the mid-manubrium and the lateral process, the inferior-tip of the incus, the anterior crus of the stapes and the anterior footplate. The displacements at these eight locations were computed at each measurement frequency in each specimen.

Frequency-dependent averages of the point motions from the three ears with an intact ISJ were computed. Since (as discussed later) the measurements made in the different ears were not made at all the same frequencies, we interpolated each data set to a fixed frequency array and the interpolated complex values from multiple ears at each frequency were averaged. The fixed frequency array included 50 frequencies logarithmically spaced between 0.4 and 20 kHz. The magnitudes of the interpolated point displacement measurements in the different ears were averaged in the log-domain (geometric averaging), while the average phase angles are the phase of the complex average of the interpolated displacement transfer functions.

Smoothed two-dimensional motion maps (in x and y) of the lateral surfaces of the ossicles (Figs. 6–8) were also constructed. The motion (magnitude and phase) of all the points contained within the previously identified two-dimensional surfaces were smoothed by rolling window (3×3) complex averaging.

2.5. Specimen preparation

All animal measurements were performed with the approval of the Animal Care Committee of the Massachusetts Eye and Ear. Measurements were made in the middle ears of six cadaveric chinchillas (that had been previously used in other live-animal experi-

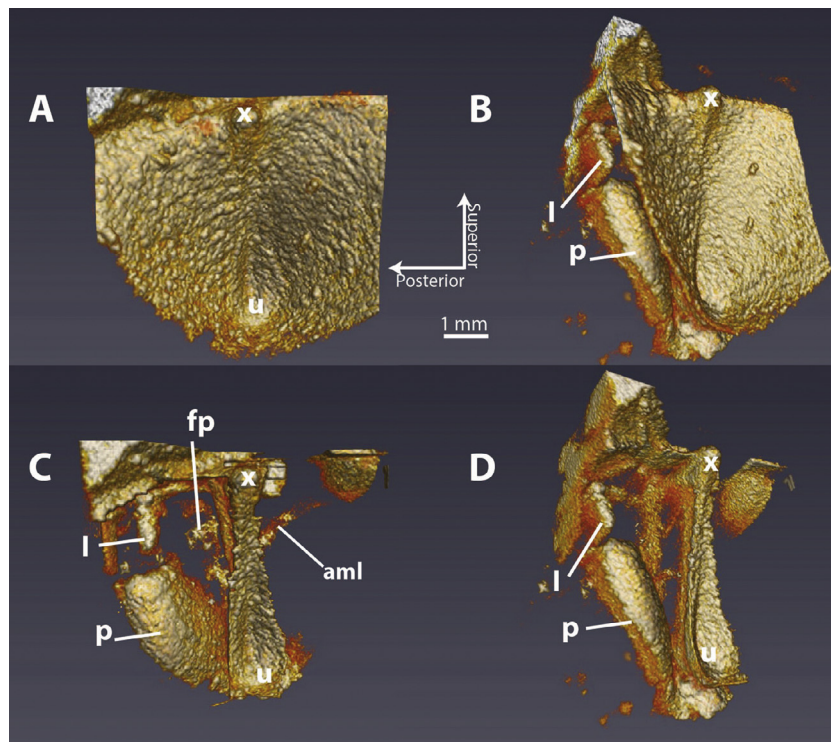


Fig. 3. Four three-dimensional surface reconstructions of the 128 B-scans from the right ear of CH2. (A) and (C) are face-on views of the lateral surface of the TM and ossicles where the z-axis is perpendicular to the page. (B) and (D) show the same reconstructions after tilting the posterior-anterior axis 20° to visualize better the structures behind the posterior TM. (C) and (D) are like (A) and (B) but after removing the free-standing TM from the reconstruction. The segmentation of the manubrium and free-standing TM was aided by looking at the sound-induced motion of these structures at frequencies above 10 kHz, where previous data have shown the manubrium moves out of phase with the TM (Cheng et al. 2013). The labeled structures include: x – the lateral process of the malleus, u – the umbo of the malleus, I – the inferior tip of the incus, p – the petrous bone, fp – the surface of the footplate, and aml – the anterior-malleal ligament (Vrettakos et al. 1988). Movies of rotating reconstructed TM and ossicular surfaces are included in Supplementary Materials 2, 9 & 10.

ments), whose heads were either stored in saline at 4 °C for 1 or 2 days, or frozen (for up to a month) and thawed prior to measurements. Three of these animals were used in developing our methods; the results from three right ears and one left ear from three animals are described. Cadaveric material was used to prevent any large extraneous displacements of the TM and ossicles due to breathing or heartbeat. The use of cadaveric material also simplified the placement of the ear within the imaging system.

The cartilaginous ear canal was removed, and the bony canal drilled away to provide a view of 75 to 80% of the TM surface; further drilling endangered the support of the TM in the ear (see Supplemental Material 1). In removing the bony ear canal, it was necessary to remove the thin dermal layer on the exterior (lateral) surface of the TM. (Previous holographic measurements (Rosowski et al. 2009; Cheng et al. 2013) of sound-induced motion of the TM suggest removal of the dermis has little effect on TM motion, and our OCT-based measurements of sound-induced ossicular displacement are quite similar to measurements made in live ears, see Results Section.) Posterior and superior openings were made into the middle-ear air cavity to allow us to cut the tendon of the tensor tympani, determine the condition of the ossicular chain, and moisten and remove excess fluid from the middle ear (Rosowski et al. 2006). The tendon of the stapedius muscle and other ossicular ligaments were kept intact. The openings into the middle ear were sealed with silicone impression material just before each measurement session. The quality of the seal prevented sound from entering the middle-ear air spaces directly, but allowed the venting of any static pressure within the middle-ear cavity. Sealing also helped keep the middle ear moist.

A metal bar that ran along the anterior-posterior direction was attached to the vertex of the skull with screws and dental cement.

The bar was placed in a multi-direction manipulator to position the head in the OCT system. The head was positioned to view as much of the ossicular system through the TM as possible. This included a small (20°) rotation of the normally positioned head around the anterior-posterior axis to provide a view of the stapes and a better view of the inferior incus (see Supplemental Material 1). This rotation reduced the TM surface visible to the OCT to ~45%; however, the view included the entire manubrium of the malleus, the inferior third of the incus and the anterior crus and footplate of the stapes. The rotation also brought the measurement direction closer to the line directed from the center of the footplate through the center of the stapes head (see Supplemental Material 1.2). The medial end of a brass sound coupling tube (~2 cm long and 1 cm in diameter) was sealed to the remnants of the bony ear canal. The coupling tube had two side tubes: one to position a calibrated probe microphone (an Entymotic ER7) near the edge of the TM, the other was coupled to the earphone via a flexible tube. The lateral end of the coupler was sealed by a glass plate that allowed access of the OCT measuring beam to the TM and middle ear.

2.6. Anatomy-based definitions of motion directions

Our measurements and analyses allowed us to describe the motions of the ossicles in one translational and two rotational directions. In doing so we used an anatomically-based geometry. As described above and in Supplemental Material 1.2, the beam of the OCT was directed along lines that roughly parallel the line connecting the center of the stapes head and the center of the footplate. This direction defined the lateral-medial direction or z-axis. The superior-inferior direction (y-axis), which approximately paralleled the arm of the manubrium, and anterior-posterior directions

(x -axis) were defined as orthogonal to the lateral-medial direction and were consistent with the changes in beam location produced by the paired galvanometers.

2.7. Acoustic Stimuli

The sound stimuli were continuous pure tones of 10 to 20 selected frequencies that were sub-harmonics of the 45 kHz wavelength-sweep repetition rate. The stimulus frequency equaled $(45,000 \times n/m)$ Hz, where m defined the number of consecutive A-line samples at each x, y position, and n defined an integer number of stimulus cycles time-locked to the m A-lines. With $m = 200$ (its value in CH2, 3 and 4), as n varied from 2 cycles for recorded waveform to 100 the stimulus frequency varied between 450 Hz and 22.5 kHz. Since, the number of x and y points in each spatial scan was $128 \times 128 = 16,384$, if $m = 200$, then over 3 million A-lines were gathered during each stimulus presentation, and a stimulus duration of about 73 s was needed to measure the motion of the entire three-dimensional volume.

The first measurement was performed at a frequency, near 0.5 or 1 kHz. Subsequent measurement frequencies were randomized, though the final measurement was a repeat of the first frequency, and occasional multiple level measurements were performed at select frequencies. We did not make reliable measurements at all possible frequencies in each ear due to either time restrictions, or the inadvertent use of stimulus levels at selected frequencies that produced displacements too large to measure accurately (see below). The plotted symbols on the individual data curves included in Figs. 4B–D and 5B are the frequencies where reliable measurements were performed, these included nine measurements at seven frequencies in CH1, 16 measurements at 13 frequencies in CH2, 13 measurements at 12 frequencies in CH3 and 12 measurements at 11 frequencies in CH4.

Stimulus-synchronous sampling of the output of the calibrated probe-tube microphone defined the magnitude and phase of the sound stimulus. The level of the tonal stimuli was varied between 80 and 120 dB SPL to produce displacements that were larger than the 10 to 20 nm noise floor of our methods (Ramier et al. 2018a), and smaller than the $\sim 0.5 \mu\text{m}$ displacements that produced interference phase differences larger than a half-cycle (such large phase differences were not easily translated to displacement).

3. Results

3.1. Observations of ossicular structure through the intact TM

As described in the methods, the magnitude of the Fourier transform of each wavelength sweep of the OCT produced an A-line that defined the reflectance and location of structures along the z -axis described by laser beam. The two-dimensional position of the A-lines was scanned in x and y using the paired galvanometers. Fig. 2 illustrates a set of A-lines scanned in x (the anterior-posterior dimension, what are called B-scans) at six specific y (the superior-inferior dimension) values. The structures observed in each scan are described in the figure caption. A significant limitation of these images is that the B-scans only resolve regions of the TM and ossicles that are visible to the OCT beam, where the presence of ear-canal bone lateral to the TM or ossicles blocks the OCT beam thereby limiting visibility behind the bone. The limitation is responsible for the truncation of the image in the anterior-posterior dimension in the 110th B-scan, and the limited lateral-medial depth in the 8th B-scan. Another limitation is that bony structures scatter as well as reflect incident light, where the former process causes the lighter gray ‘fork-like’ projections medial to the manubrium seen in B-scans 36, 45 and 67. This scattered light is often associated with a darker shadow region medial

to the scattering bone seen in the most medial reaches of those same three B-scans.

Stacks of the 128 B-scans ordinarily arranged in y were used to reconstruct the three-dimensional structure of the ear. Fig. 3 shows different views of two reconstructions of the lateral surfaces of the TM, ossicles and surrounding bone in one ear, including face-on views of the TM and the middle ear and bony structures behind the TM, as well as images of those same structures after rotating the ear by 20° about the superior-inferior axis. (Brief movies of rotations of the reconstructions are included as Supplemental Material 2.) Images in which the free-standing TM was segmented and removed from the reconstructions (Figs. 3C and D) clearly show the TM-covered manubrium of the malleus, the inferior tip of the incus, and the petrous bone that covers the basal and middle turn of the cochlea. The stapes crus and footplate are not clearly seen in these images due to the intensity-based thresholding algorithm used to reduce noise in the image of the manubrium and incus.

The presence of the medial wall of the bony ear canal at locations superior to the lateral process prevented observation of the head of the malleus and the body of the incus (see Supplemental Material 2). Nonetheless, the image in Fig. 3C is very similar to the scanning-electron-microscope image of the chinchilla ossicles and petrous bone with the TM and ear-canal wall removed published as Fig. 2 in Vrettakos et al. (1988), and the micro-CT-based reconstructions of Wang and Gan (2016), though those images include the heads of the malleus and the incus. Measurements of the length of the manubrium (~ 4.5 mm) and the height of the stapes (~ 2 mm) gathered from reconstructions of our specimens are consistent with those of Vrettakos et al. (1988) and Wang and Gan (2016). A lack of definition of the complete TM, incus lever arm and stapes footplate prevented assessment of the dimensions of these structures in our data set.

3.2. Point measurements of sound-induced motion: Normalization by stimulus sound pressure

Displacement-to-sound pressure transfer functions – complex ratios of the frequency-dependent sound-induced displacement and measured sound pressure – at three specific ossicular locations (Fig. 4A) are illustrated in Fig. 4. The figure describes the magnitude and phase-angle of transfer functions for the sound-induced displacement of the umbo, the inferior-most tip of the incus and the anterior stapes footplate. The plots also compare these transfer functions to previous studies. The transfer functions were measured in 4 ears, and include one ear (CH4) in which the incudostapedial joint (ISJ) was accidentally interrupted during preparation. Fig. 4B illustrates the measured umbo displacement to sound pressure transfer function in the 4 ears, along with the averaged magnitude and phase from the three ears with an intact ossicular chain. The average umbo displacement to ear-canal sound pressure transfer function reported by Ruggero et al. (1990) – made with the middle-ear cavities sealed – is also plotted. Fig. 4C is a similar comparison of our incus to sound pressure transfer functions and those reported by Robles et al. (2015), while Fig. 4D compares our footplate displacement to sound pressure transfer functions to averages reported by Ruggero et al. (1990) and Robles et al. (2015).

The magnitudes of the individual displacement transfer functions we measured at the umbo, incus and stapes footplate in the three specimens with intact ossicular chains vary by as much as an order of magnitude at frequencies less than 6 kHz, but vary less at higher frequencies. The variations in phase angle between the three individual transfer function phases is about 0.25 cycles throughout the frequency range. Some of this variability may come from differences in the location of the P_{EC} measurements in the different ears, as the probe tube was placed at the outer edge of the ear canal at distances from the umbo greater than 5 mm,

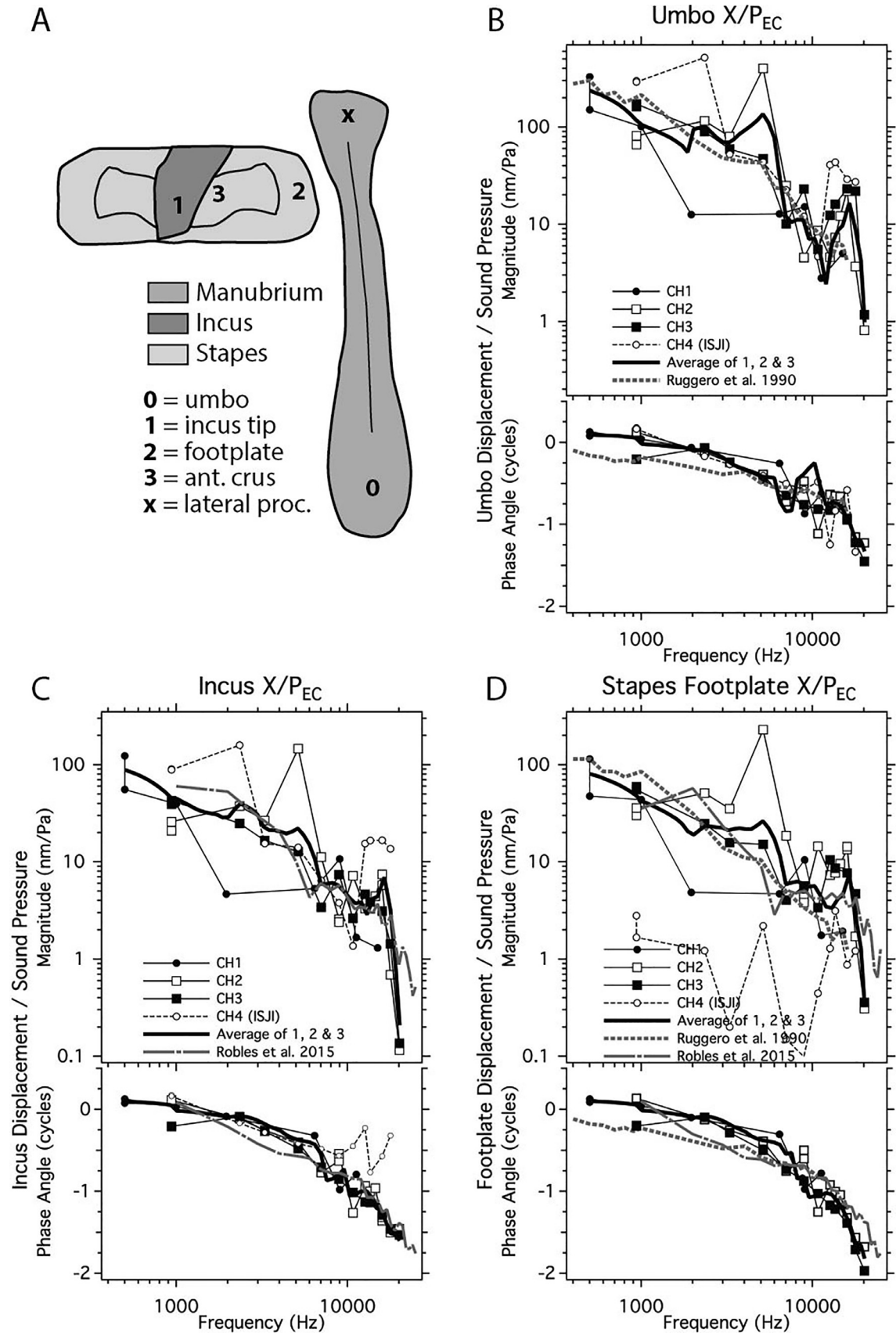


Fig. 4. Transfer functions between the sound-induced displacement and stimulus sound pressure in 4 cadaveric chinchilla ears at three ossicular locations labeled in (A), including: the umbo (B), incus tip (C) and stapes footplate (D). The upper panel of each plot describes the magnitude (units of nm/Pa), and the lower panel describes the phase angle. The magnitudes and phase angles are plotted on a log-frequency scale. Symbols mark the frequencies were measurements were made in individual ears; repeated measurements at any one frequency are marked by paired symbols. The thick solid lines in the upper and lower panels represent the complex average of transfer functions in ears CH1, CH2 and CH3. The measurement in CH4 with the incudostapedial joint interrupted (ISJI) is not included in the average. Our measurements are compared to the means of measurements of [Ruggero et al. \(1990; N = 5\)](#) and [Robles et al. \(2015; N = 5\)](#).

where this distance depended on how much ear canal was removed and varied with each preparation. Despite this variability, the average transfer functions are similar to those reported by [Ruggero et al. \(1990\)](#) and [Robles et al. \(2015\)](#).

The umbo and incus displacement transfer functions in CH4 with the ISJ interrupted are not obviously different from those of the other three ears, except for the magnitude and phase angle of the umbo and incus transfer function at frequencies at 2250 Hz and above 10 kHz. As interruption of the ISJ eliminates the coupled motion of the stapes and the malleus and incus, the magnitude of the stapes footplate transfer function in CH4 is a measure of the combination of stimulus-induced motion of the whole head and displacement noise, and is generally at least a factor of 3 lower than the transfer-function magnitudes in the other ears at sound stimuli of frequencies less than 18 kHz. (Exceptions are in CH1, where the magnitude at 11 and 15.9 kHz are less than the magnitude in CH4 at 13.6 kHz.) Subsequent plots of these point displacements are restricted to data below 18 kHz.

3.3. Point measurements of sound-induced displacement: Relative motion along the ossicular chain

Of primary significance in this report are relative motions within the ossicular chain of the chinchilla. [Fig. 5](#) includes the data of [Fig. 4](#), but shows the ratios of the complex sound-induced displacement of discrete points on the ossicular chain to the displacement measured at two reference points, either the umbo, or a position $\frac{3}{4}$ up the manubrial arm. The curves plotted in the figure are smoother and less variable than the displacement to sound pressure ratios plotted in [Fig. 4](#). The smaller variability in the umbo-normalized data ([Fig. 5](#)) is consistent with our suggestion that part of the variation observed in [Fig. 4](#) was due to inter-individual variations in the sound-pressure measurements.

[Fig. 5B](#) plots the magnitude and phase angle of the footplate-to-umbo displacement ratio in the three ears with an intact ISJ, along with the average of the three ratios and the footplate-to-umbo displacement ratio computed from [Ruggero et al. \(1990\)](#). While similar below 3 kHz, the magnitudes of the ratios we describe are on average a factor of 2 to 3 higher than that reported by [Ruggero and co-workers](#) at frequencies between 5 and 15 kHz. The phase angle of the displacement ratios is quite similar in all of the plotted measurements, especially at frequencies above 10 kHz, where all of the data sets show a rounded step of negatively accumulating phase in the log-frequency domain that reaches a value of about a negative half cycle at 15 to 18 kHz in the new data.

[Fig. 5C](#) plots the averaged umbo-normalized motion magnitude at 4 manubrium locations, including the lateral process and at $\frac{1}{4}$, $\frac{1}{2}$ and $\frac{3}{4}$ of the length between the lateral process and the umbo. The variation within the individual measurements used in the means is similar to that observed in [Figs. 5B&E](#). At all of the measured frequencies the umbo motion (represented by a magnitude of 1 and phase angle of 0 in this ratio plot) is larger than that at any other plotted location, and all of the data are consistent with reduced motion magnitude as the measurement locations moves up the manubrial arm to the lateral process. The motion relative to the umbo at the four points also varies with frequency, especially at the two most superior points. The motion relative to the umbo moves closer to one between 2 and 10 kHz, with a decrease in the relative magnitude above 10 kHz at all locations, and a suggestion of a rebound above 15 kHz in the relative magnitude and phase angle at all manubrial locations. The four points generally move in phase with the umbo, except between 8 and 18 kHz, where phase lags of as much as 0.2 periods develop, with larger phase lags at greater distances from the umbo.

[Fig. 5D](#) plots the average of the displacement ratios measured in the three ears at different points along the ossicular chain: mid-

manubrium, lateral process, the inferior incus tip, the stapes anterior crus and the anterior footplate. The ratio of the displacement of the mid-manubrium and the umbo has a magnitude near 0.6 below 10 kHz and is generally the largest of the ratios. The displacement of the lateral process is 20 to 30% of the umbo displacement at all but the highest frequencies, and is the smallest measured motion at any frequency. The displacements of the inferior incus tip, stapes anterior crus and stapes footplate have similar magnitudes that fall between that of the mid-manubrium and lateral process at frequencies less than 10 kHz. At higher frequencies the stapes footplate moves more than all of the other points, with the exception of the mid-manubrium at frequencies above 16 kHz. The phase-angles of all the plotted ratios show a smoothly increasing phase delay between 8 and 13 kHz, where the phase grows more negative as the measurement location progresses from mid-manubrium to lateral process to incus tip to stapes anterior crus, and is most negative at the footplate near 15 kHz where it reaches about -0.5 cycles.

[Fig. 5E](#) plots the ratio of the footplate to the $\frac{3}{4}$ manubrium position in our three ears along with the mean of these measurements. At frequencies below 7 kHz, the footplate motion is similar to the motion at the $\frac{3}{4}$ manubrium position in both magnitude (within about $\pm 30\%$) and phase angle (within about ± 0.05 periods). All three of the individual ratios show a moderately sharp peak in magnitude of 2.5 to 4 near 14 kHz, with a corresponding phase step of near 0.4 periods. Between 15 and 18 kHz, the phase in all three individuals shows more delay and the magnitude returns toward 1. The peak magnitude and phase change in the individual ears are well represented by the mean.

3.4. Spatially continuous measurements of sound-induced ossicular displacements normalized by the displacement of the umbo

While the previous section concentrated on the motion of individual points along the manubrium, a primary benefit of OCT is the ability to scan our measurements over the entire visible ossicular surface with a high degree of spatial selectivity. [Fig. 6](#) illustrates the umbo-relative displacement magnitude and phase angle measured along the lateral surface of the three ossicles in response to a ~ 1 kHz tone in four ears. Each row illustrates the data from 1 ear. The left-most column uses colors to illustrate the umbo-relative displacement magnitude, where a magnitude of 1 is a mid-yellow and 0 is deep blue. The center column shows the phase angle of the displacement relative to the displacement of the umbo. The right most column is a repeat of the magnitude data with labels to distinguish different locations along the ossicular chain.

The results with 1 kHz stimulation include: (i) There is a graded magnitude of sinusoidal motion along the manubrial arm, where the umbo-relative motion magnitude is greatest (~ 1.1 , bright yellow) at the inferior tip of the manubrium and least at the superior end (~ 0.2 , blue) above the lateral process. (ii) The magnitude of the motion of the incus and stapes (~ 0.3) is similar to the motion of the manubrium at a similar superior-to-inferior distance from the lateral process (e.g., the $\frac{3}{4}$ position, see [Fig. 5E](#)). (iii) Motion isoclines (described by the color gradations) seen on the manubrium are arranged perpendicular to the long axis of the manubrium. (iv) All points on the surface of the ossicles move approximately in phase with the umbo (the color is constant at medium blue green). These patterns are apparent in all four ears regardless of whether the ISJ is intact or interrupted (the bottom row of panels in [Fig. 6](#)), and are consistent with the point motions plotted at 1 kHz in [Fig. 5](#). As will be described in the discussion, these motion patterns are also consistent with ossicular rotation about an axis that is perpendicular to the long axis of the manubrium, and superior to the lateral process.

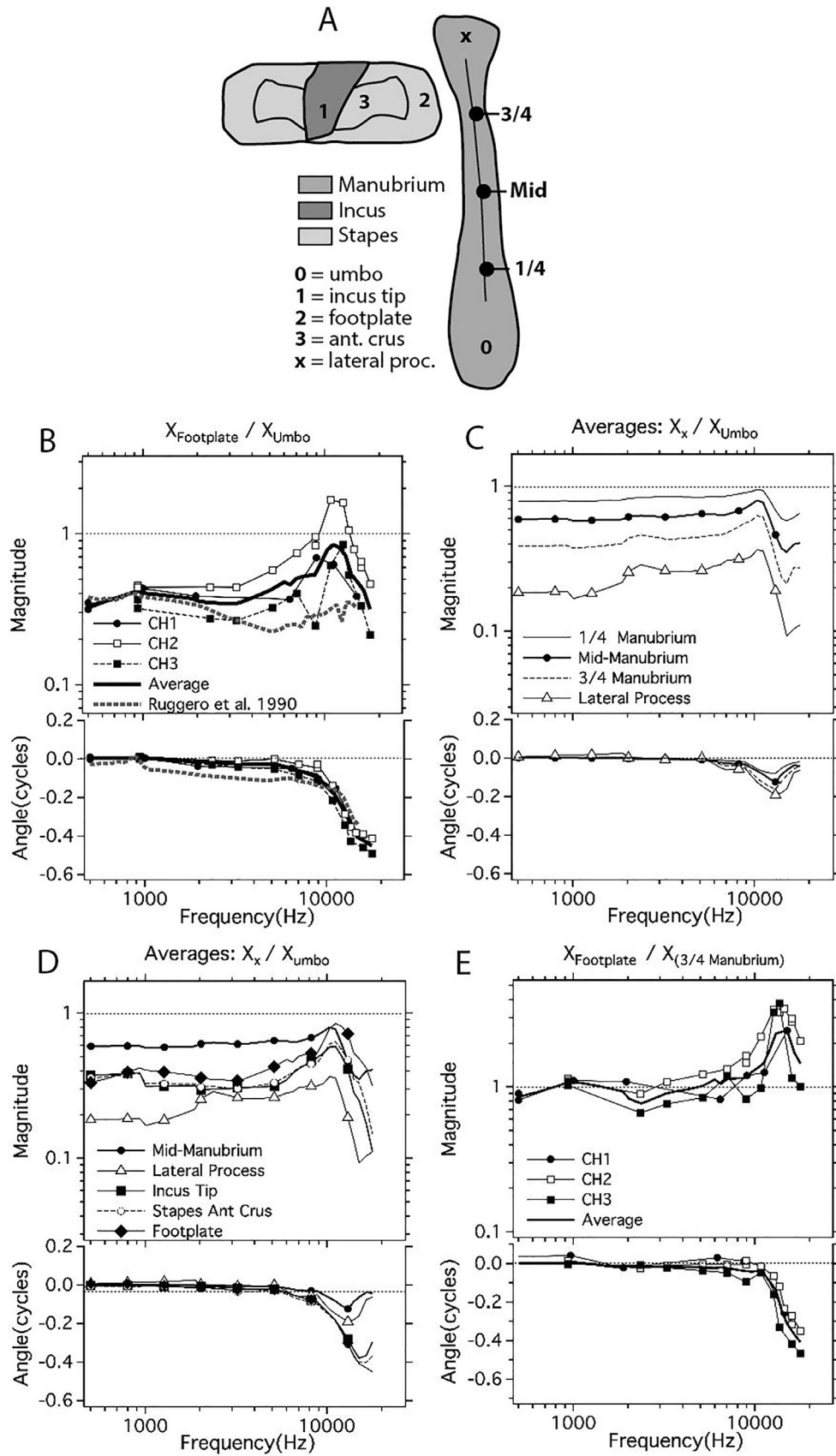


Fig. 5. Ratios of the measured motions at eight different ossicular locations (A) in the three ears with an intact ISJ. (B) The magnitude and phase angle of the ratio of the measured displacements of the stapes footplate and umbo. The average of the three measurements is included, as is a similar measurement by *Ruggero et al. (1990)*. (C) Averages of the umbo-normalized displacement measured at 4 locations along the long axis of the manubrium specified by the fraction of the distance between the umbo and the lateral process. (D) Averages of the umbo-normalized displacement measured at five different ossicular locations. (E) Individual and average measurements of the ratio of the displacement of the stapes footplate and the position 3/4 along the manubrium.

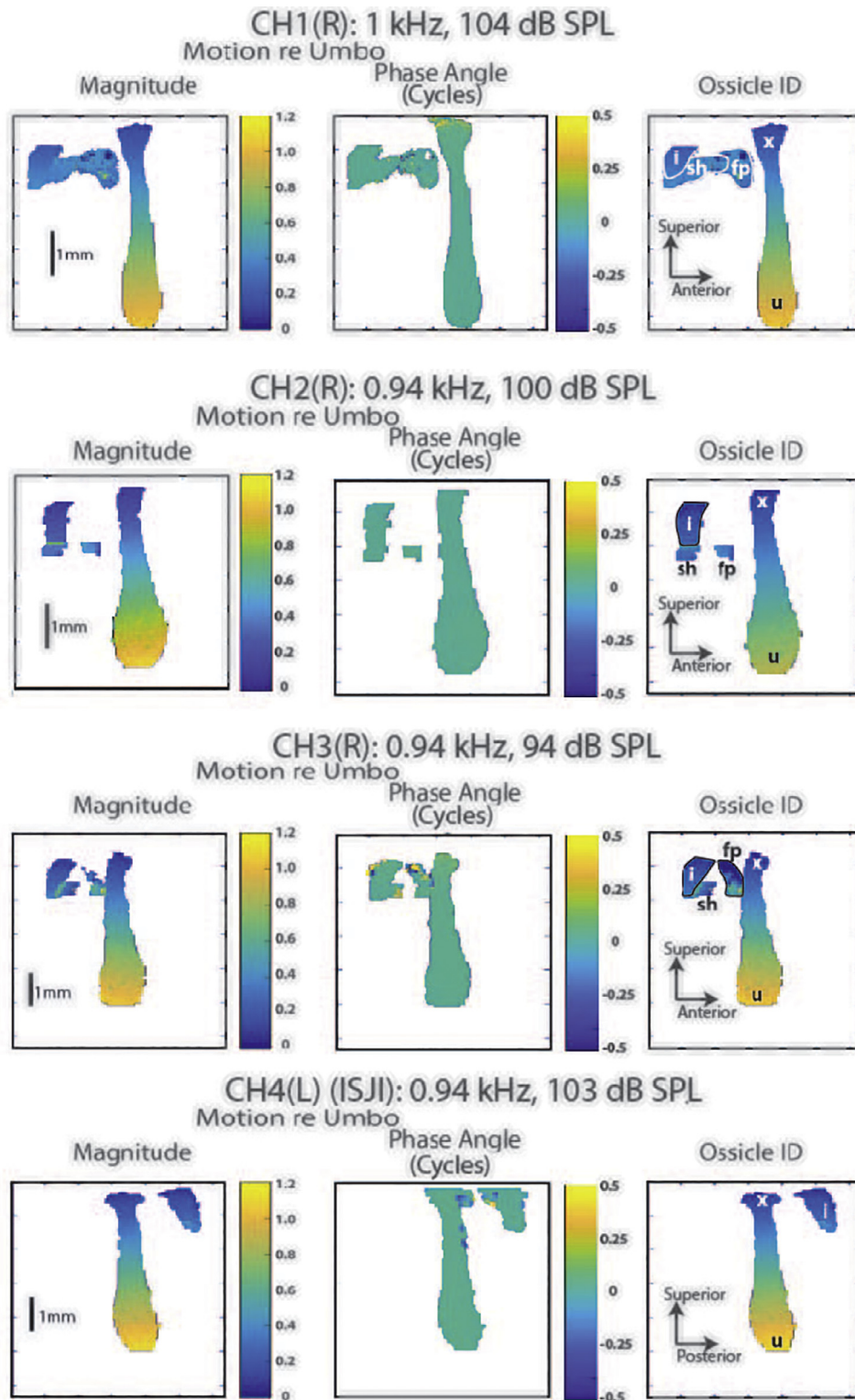


Fig. 6. Two-dimensional views of the magnitude and phase angle of the OCT determined sound-induced displacement of the OCT-visible lateral surfaces of the ossicles normalized by the displacement of the umbo in four ears. Stimuli were tones near 1 kHz of levels near 100 dB SPL. Variations in the relative distance and the 3D-rotation of the ears relative to the OCT beam produced small differences in scale and orientation. The third column identifies the umbo (u), the lateral process of the manubrium (x), the incus (i), stapes head and anterior crus (sh) and stapes footplate (fp). The visibility of the structures depends on the intensity of the reflected light and the existence of motion above the 10–20 nm noise floor. CH1, 2 and 3 are right ears. CH4 is a left ear with an interrupted IS joint and little motion of the stapes (Fig. 4C).

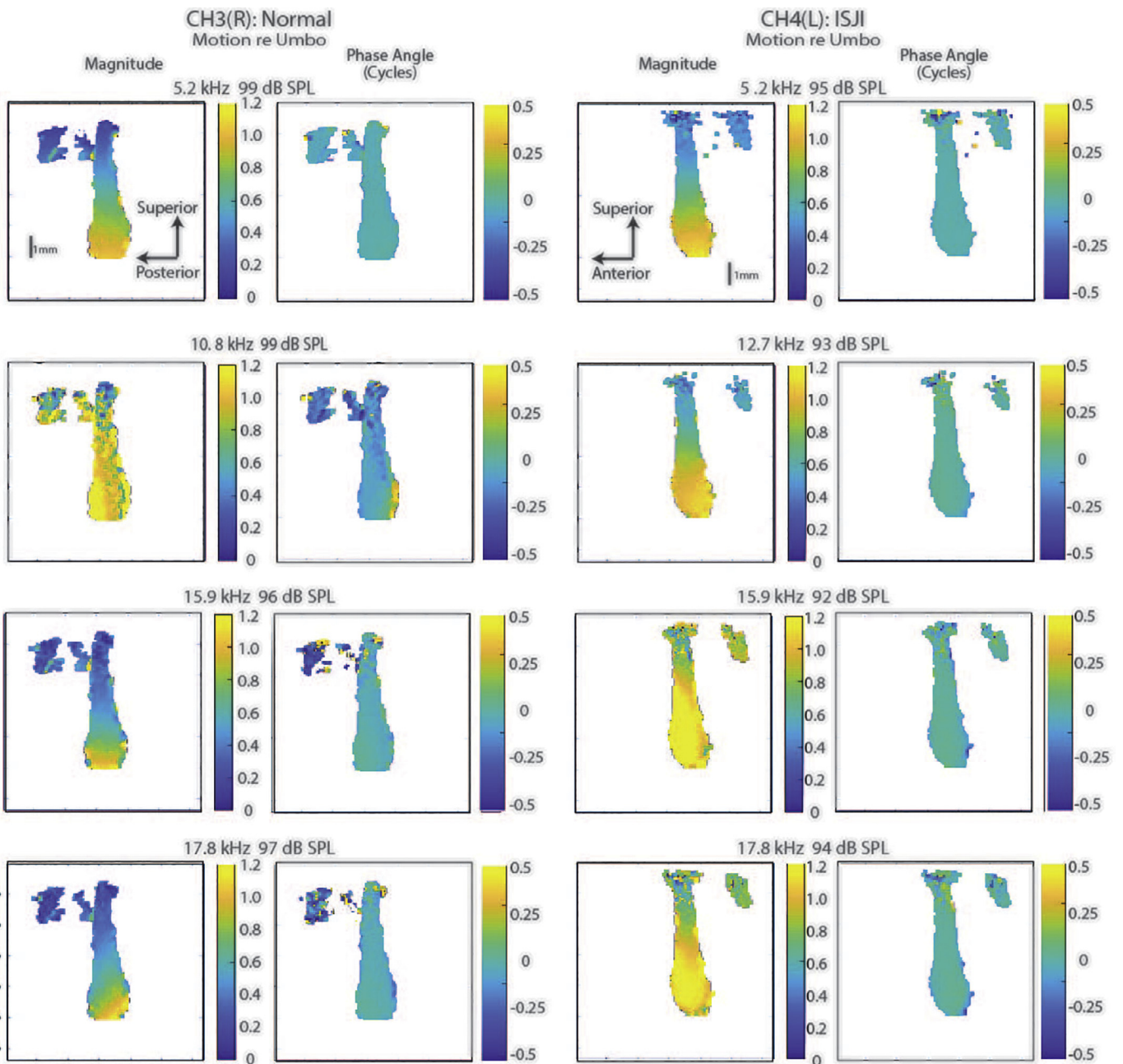


Fig. 7. Comparison of ossicular motion in two ears at four frequencies. Ear CH3 is a right ear with an intact ossicular chain and moving incus, stapes head and footplate. Ear CH4 is a left ear with the incudostapedial joint interrupted with a mobile incus, but no measurable stapes motion.

Fig. 7 shows a similar presentation of the motion of the ossicles at four frequencies between 5 and 18 kHz in two ears: one with an intact ossicular chain (the right ear CH3, the two left-hand columns) and the ear with the ISJ interrupted (the left ear CH4, the two right-hand columns). We first concentrate on the intact ear. At 5.2 kHz we again see a graded magnitude of motion along the manubrium (as was visible at 1 kHz). However, the motion isoclines are no longer perfectly perpendicular to the long axis of the manubrium, such that the motion of the posterior edge is a little larger in magnitude than the anterior edge at a similar inferior-superior location. We also see that the magnitude of the umbo-relative motion at the lateral process and the other ossicles (~ 0.3 re the umbo) is a little larger than at 1 kHz (Fig. 5B). For the most part the ossicles continue to move in phase at 5.2 kHz as they did at 1 kHz.

With a tonal stimulus of 10.8 kHz (the two left-hand panels in the second row of Fig. 7) the motion patterns in the intact ossicular chain are quite different from that at lower frequencies. Much of the manubrium, the inferior incus and the footplate is moving in the lateral-medial direction with a similar magnitude. The magnitude of the umbo-relative motion of the lateral process, incus and stapes remains comparable to that of the manubrium at a similar inferior-superior position. There is also a sign of graded motion and phase angle isoclines that parallel the long axis of the manubrium, with larger motion magnitudes on the anterior and posterior manubrial edges. Much of the manubrium moves in phase with the umbo, though the anterior-inferior manubrial rim moves nearly out of phase with the rest of the manubrium. The phase of the incus and stapes is noisy, but the average phase of motion is negative rather than zero.

With tonal stimuli near 16 and 18 kHz, the relative motion of the manubrium has more in common with the motion at 6 kHz and lower, with graded motion magnitudes along the inferior-superior orientation of the manubrium, and nearly-in-phase motion of the entire manubrial surface. However, there are significant deviations from low-frequency behavior. (i) The gradations in manubrial magnitude are not as evenly arranged in the inferior to superior direction, such that the relative motions of the superior portions of the manubrium are of smaller magnitude than those at 1 kHz. (The moderate blue region begins 1/3 of the distance from the lateral process at 15.9 kHz, and at a position of ¼ the distance at 1 kHz). (ii) The isoclines of relative motion magnitude are less horizontal. (iii) The largest difference compared to lower frequencies is that the incus and stapes move nearly half-a-cycle out-of-phase with the umbo and the manubrium. Maps of the motion of the ossicles in two other ears are included in Supplemental Material 3. All of the patterns of relative motion of the ossicles described in Figs. 6 and 7 are also visible in short movies of the sinusoidal motion of the ossicular surfaces in Supplemental Materials 4 through 8.

3.5. Spatially continuous measurements of sound-induced ossicular displacements normalized by the displacement of the umbo at mid to high frequencies with the ISJ interrupted

Fig. 6 demonstrates that interruption of the incudostapedial joint produced little difference in the relative motions of the malleus and incus in response to a near 1 kHz stimulus. The right two-columns of Fig. 7 demonstrate ISJ interruption was associated with significant differences in the relative ossicular motion at higher stimulus frequencies. At 5.2 kHz, the two upper right-hand panels in Fig. 7 demonstrate some similarities to the motion patterns of Ear CH3: (i) There is a graded magnitude of motion that is largest near the umbo and smallest at the lateral process. (ii) The magnitude of incus motion is similar to the motion of the manubrium at a similar-superior-to-inferior distance. (iii) The entire manubrium and the visible incus move in phase. A difference between the motion in CH4 at 5.2 kHz (Fig. 7, top right panels) and ears with the ossicles intact is that the relative motion of the lateral process and incus is larger after ISJ interruption (the motion magnitude is ~0.5 -middle-to-light blue- in the ISJ case and ~0.2 -middle-to-dark blue- in the normal ear).

At 12.7 kHz in the ISJ ear, the two-right-hand columns in the second row of Fig. 7, we again see graded motion magnitude and in-phase motion, but even larger relative motions of the superior portion of the manubrium and the incus. At 15.9 and 17.8 kHz in the ISJ interrupted ear (the two lower rows of the two right-hand columns of Fig. 7), much of the manubrium moves with a magnitude similar to the umbo, though the superior 1/3 of the manubrium and the incus move with a somewhat lower magnitude (~0.8). While we observe these magnitude differences, the entire length of the manubrium and the incus generally move in phase with each other at all frequencies, in contrast with the higher-frequency out-of-phase behavior observed in the ears with an intact ISJ.

3.6. Finer variations in the relative phase of motion along the manubrium

The phase-angle color scale of Fig. 7 enables detection of relatively large (± 0.25 cycles) differences in the phase of motion within the ossicular chain, but is insensitive to smaller changes that occur in the phase of manubrial motion. To better detect such changes, Fig. 8 shows a finer-scale representation of the phase of manubrium motion relative to the umbo in all four ears. In the ears with intact ossicular chains (CH1, CH2 and CH3), the most

obvious deviations from 0 phase is the development of phase lag (more negative relative phase) at manubrial positions more superior to the umbo, with the largest changes (~ 0.2 cycles) observed at the most superior positions with the higher stimulus frequencies. The phase changes with position occur over a larger extent of the manubrium in the middle frequencies, and are less obvious at the highest stimulus frequencies. Such accumulation of phase lag is consistent with a bending of the manubrium. At the frequencies where we observe such accumulation, we generally see an increase in the grading of the magnitude with distance along the manubrium where the umbo-relative motion of the lateral process is smaller than at lower frequencies (Figs. 5 and 7), which is also consistent with bending. In the ear with the ISJ interruption, we do not see such phase accumulation along the manubrium as frequency increases (Fig. 8). Instead there is a tendency for the phase of motion at more superior points to lead the phase of motion at the umbo.

4. Discussion

We have used OCT 'volume-scanning' of the chinchilla middle ear to assess the structure and measure the sound-induced motion of a large fraction of the chinchilla ossicular chain through the intact tympanic membrane, including the entire manubrium of the malleus, the inferior half of the incus and the anterior regions of the stapes. The displacement measurements were performed by synchronizing the timing of the OCT A-lines with tonal acoustic stimuli to define stimulus-induced displacements in regions with high OCT reflectance.

4.1. Benefits and limitations of OCT measurements of sound-induced motion

The primary benefit of the use of wavelength-swept OCT to measure sound-induced motions of middle-ear structures is the ability to observe simultaneously the structure and measure the localized displacement of ossicles behind the intact tympanic membrane. This benefit is attained by: (i) the use of tissue penetrating light as a 'non-contact' sensor, (ii) the use of the magnitude of the FFT of the frequency-modulated interference pattern described by each A-line to define regions of significant reflectance associated with specific z locations with 7.8 μm accuracy, (iii) the ability to measure the motion of specific structures with a displacement sensitivity on the order of 10–20 nm by comparing the interference phase defined by the FFT at high-reflectance z locations at different times, where the high-frequency limit of such measurements is less than half of the 45 kHz A-line rate, and (iv) the ability to rapidly scan the OCT A-lines in x and y to describe the three-dimensional structure and one-dimensional displacement of much of the ossicular chain.

While the benefits are substantial, our use of an OCT beam swept in the two directions orthogonal to the OCT A-lines also has limitations. The most significant limitation is the 0.36 s needed to sample the 128×128 x - y grid to perform a single volumetric scan and the 72 s needed to assess the stimulus-induced motion along the entire x - y grid. These sample durations preclude accurate measurement of sound-induced displacement and limit measurements of structure in living, breathing animals, as respiration-induced displacements of the TM and ossicles (at frequencies of 0.1–4 Hz) can be tens to hundreds of μm . The presence of such large displacements during a volumetric scan will interfere with the accurate characterization of the spatial dependence of sound-induced motion and degrade the accuracy of the three-dimensional structural measurements. This limitation can be eased – if not eliminated – by drastically shortening the sampling period through reductions in the number of spatially and temporally varying samples in any

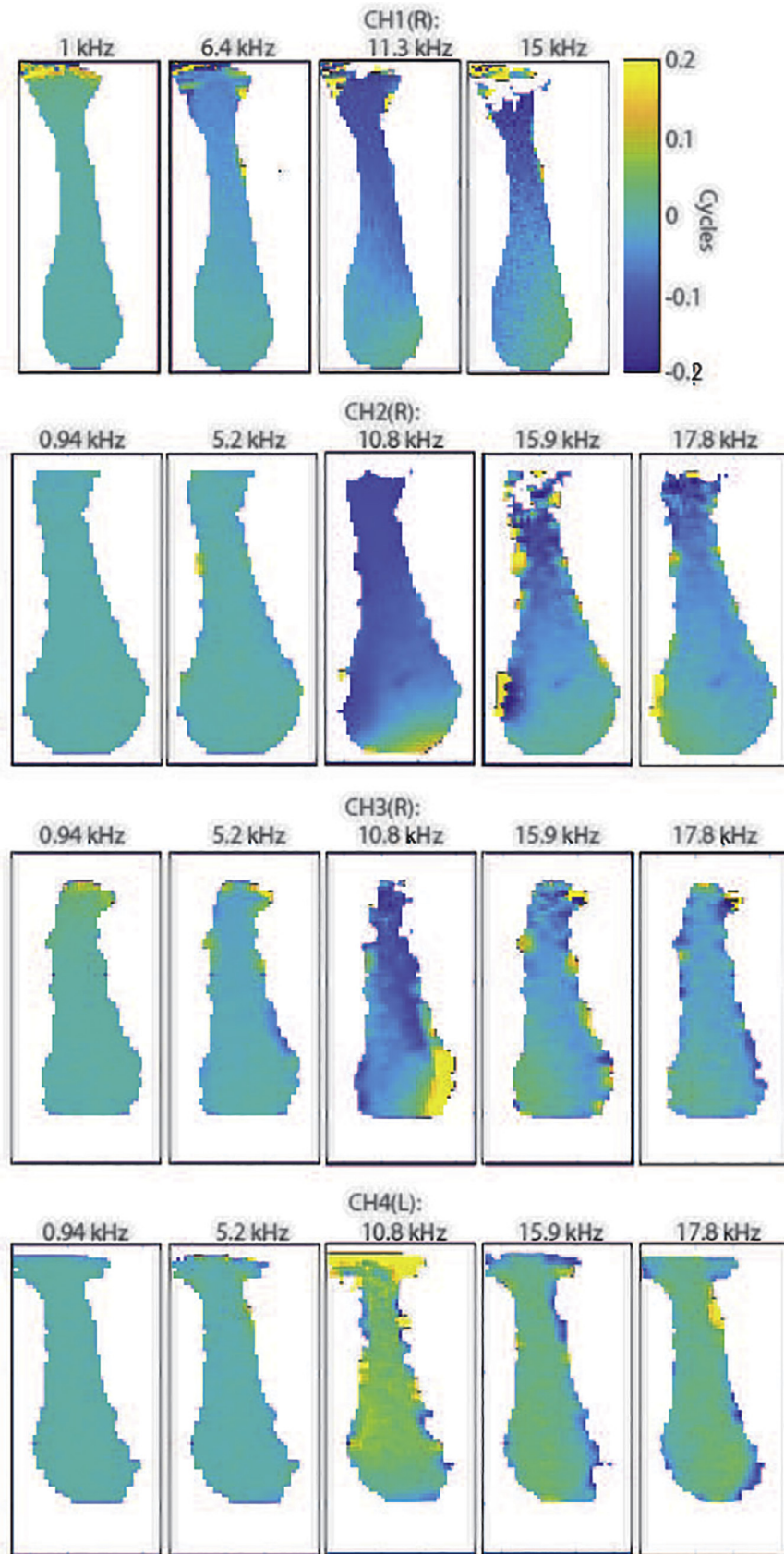


Fig. 8. Identification of smaller deviations in the relative phase of motion of the lateral surface of the manubrium. Phase maps, with a more sensitive color scale, are illustrated for the four ears at frequencies between 5 and 18 kHz.

one measurement. For example, MacDougall et al. (2016) use a rapid OCT structural scan to define several isolated ossicular locations in the middle ears of live humans (e.g., the umbo and inferior incus), then use short temporal measurement series to quantify sound-induced displacements at those locations. Such reductions in the spatial and temporal sampling density would limit our description of variations in the sound-induced motion along the ossicular chain, and were not employed in this study.

A second limitation is the restricted dynamic range of the present displacement measuring system. Our OCT system uses temporal difference in the measured interference phase at single locations (within a single voxel) to reliably measure displacements as small as 10–20 nm (Ramier et al. 2018a), but it is limited in its ability to differentiate displacements that produce interference phase differences larger than half a cycle (larger than half of the wavelength of laser light, ~500 nm). To help ensure the displacements we measure fell within our working range, we made preliminary measurements of the motion of the isolated umbo to choose appropriate stimulus sound levels. This umbo-based stimulus scaling worked well for most measurements of ossicular displacement, but produced motions of the free TM surface that were larger than the upper limit, as the motions of the TM surface are often larger than the motions of the umbo (see Cheng et al. 2013). Thus, we have ignored descriptions of TM displacement in this report.

A third limitation is that scattering and shadowing of the OCT beam restricts measurements of structures directly beneath structures with high reflectance; therefore, it is impossible to observe structures or motions behind bone that is more than a few tenths of mm thick, e.g., the bone that supports the TM hides the malleus head and incus body from view.

A fourth limitation is that our displacement measurements are one-dimensional, the OCT technique is only sensitive to displacements in the direction of the laser beam, i.e., the lateral-medial z direction defined by each measured A-line, while it has been clearly demonstrated that the ossicles respond to sound with motions in three dimensions (e.g. Decraemer et al. 1991, 2014; Decraemer and Khanna 1994). This significant limitation is ameliorated by our near simultaneous measurements of the motion in z of a large fraction of the ossicular chain. The motion of any object in space can be broken into translation along three orthogonal directions and rotation about three orthogonal axes. While sound-induced translation of the ossicles in either the anterior-posterior (x) or inferior-superior (y) directions are not quantified by our measurements, the contributions of such motions to the motion of the stapes is believed to be small (de La Rochefoucauld et al. 2008; Lauxmann et al. 2012; Decraemer et al. 2014). Also, while rotation about a z -directed lateral-medial axis will not generate displacements in z and therefore cannot be assessed by our methods, such a rotation has not usually been considered important in middle-ear sound transduction. On the other hand, rotations about any anterior-posterior (AP) or inferior-superior (IS) directed axes can generate significant spatial patterns of displacement in z . Observations of spatial variations in the phase and magnitude of z displacements of the ossicular surface (which cannot be explained easily by motions in x or y) provide insight into the presence of such rotations, as well as the location of rotational axes oriented in those two directions.

OCT measurements complement other technologies. Scanning laser-Doppler vibrometry can measure motions with higher frequency resolution than is easily achievable with OCT, but it cannot assess the motion of the incus and stapes behind the TM or define the structure of the ossicles (Ball et al. 1997, Wang and Gan 2018). Furthermore, gathering the number of point data measurements required to adequately describe the motion of the manubrium, incus and stapes would be time consuming. Three-dimensional scan-

ning vibrometry would better describe the complex motions of the points on the ossicles, but needs to be combined with structural measurements in order to separate translation and rotational motion components, and cannot measure the motion of the structures behind the TM. Micro-CT, which is not limited by the shadowing of laser light by bone, can better describe the structure of the entire ossicular chain within the intact middle ear (e.g., Wang and Gan 2016), but cannot describe ossicular motion, is best performed on small samples, and requires multiple minutes of scanning to achieve useful resolution (e.g., Sim and Puria 2008; De Greef et al., 2015).

The best analyses of ossicular motion and structure performed to date are those of Khanna and Decraemer and co-workers (Decraemer et al. 1991, 1994; Decraemer and Khanna 1994, 2004; Decraemer et al. 2014). They employed a one-dimensional heterodyne laser with narrow depth of field to measure the sound-induced motions of the TM and ossicles in specimens with ears centered in a three-dimensional positioning device. Measurement of the motion from different angulations and the relative distance between the specimen point and the laser (based on optimizing the focus of the beam) of 40 to 80 points on the ossicular surfaces, were combined with later micro-CT based anatomical measurements of each specimen to describe the complex three-dimensional motion of the entire ossicular chain. The motions they described included translations in three dimensions, rocking, rotations and bending within the ossicular chain of cats, humans and gerbils. The time and effort necessary for those studies was much greater than the time we needed to perform our more limited but still useful descriptions of the modes of ossicular motion in chinchilla.

4.2. Chinchilla ossicular structure

Our structural measurements are consistent with the already extensive knowledge of the structure of the chinchilla ossicular system provided by others (e.g. Vrettakos et al. 1988; Ruggero et al. 1990; Robles et al. 2015; Wang and Gan 2016). Our data confirm the linear dimensions of the chinchilla ossicles are generally similar to those of human, including: manubrial lengths of 4–5 mm, stapes heights of about 3 mm, and short and long axes of the footplate of 1 and 2.5 mm. The major human-chinchilla differences include: the rigid connection of the malleus and incus, and the shorter incus lever arm and consequently larger anatomical ossicular lever ratio (2.5 in chinchilla as opposed to 1.4 in human) in chinchilla.

4.3. Chinchilla ossicular motion: Intact ossicular chain

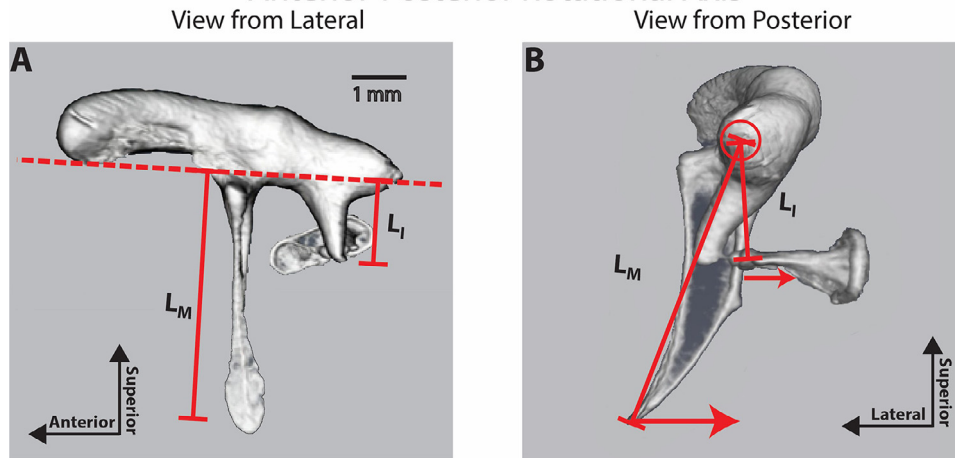
Our data suggest the existence of multiple modes of motion in the intact ossicular chain. These include: (i) rotation about an anterior-posterior (AP) directed axis, similar to that defined by the anterior process of the malleus and posterior-incudal ligaments (Fig. 9A&B), (ii) whole-body translation of the ossicles along the z -axis (Fig. 9C&D), (iii) rotation about an inferior-superior (IS) directed axis that is perpendicular to the AP axis and located near the long axis of the manubrium (Fig. 9E&F). (iv) bending of the manubrium. The evidence for each of these is reviewed in the following paragraphs. Much of what we discuss next is also visible in the brief pseudo three-dimensional movies of ossicular motion included in Supplemental Materials 4 through 8.

4.3.1. AP-rotary axis

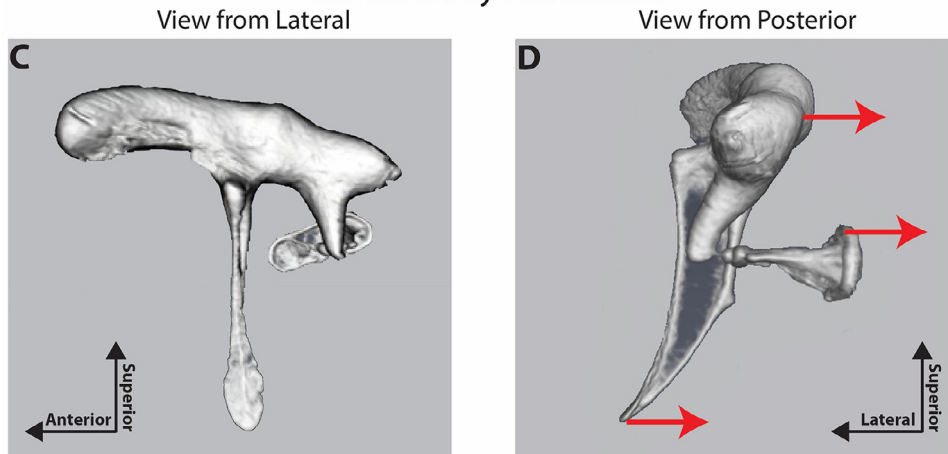
The mode of ossicular motion defined by rotation of the rigid ossicles around the anatomically defined AP axis (or some axis like it) will produce in-phase displacement of all of the structures on one side of the axis (the entire visible ossicular chain

z-Component of Motion in Different Motion Modes

Anterior-Posterior Rotational Axis



Whole-Body Translation



Superior-Inferior Rotational Axis

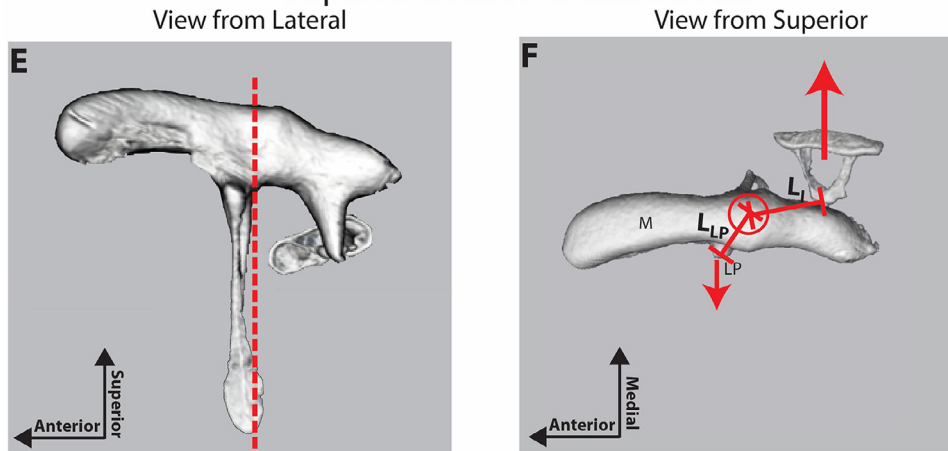


Fig. 9. Two views of three hypothetical modes of ossicular motion, each view is based on an Amira® reconstruction of microCT scans (Bowers 2020) of a chinchilla ear. **A and B:** Views from a lateral (A) and posterior (B) aspect of the motion produced by rotation around an anteriorly-to-posteriorly directed axis defined by the anterior-malleal process and the posterior-incudal ligament (the dashed line). The bracketed lines in (A&B) describe the lengths of the lever arms of the malleus (L_M) and incus (L_I). The circle in the posterior view (B) shows the approximate position of the rotational axis and the arrows describe the relative magnitude of the inward displacements of the umbo and stapes head produced by a positive sound pressure in the ear canal. **C and D:** Views from a lateral (C) and posterior (D) aspect of the motion mode produced by whole body translation in z. The arrows in (D) show the equality of motion of the entire ossicular chain produced by a sound pressure in the ear canal. **E and F:** Views from a lateral (E) and superior (F) aspect of the motion produced by rotation around a superiorly-inferiorly directed axis positioned near the posterior edge of the manubrium of the malleus. The dashed line in (E) and the circle in (F) illustrate a hypothetical position of such an axis. The bracketed lines in (F) show the lengths of the hypothetical lever arms between the axis and the lateral process (L_{LP}) and the axis and the inferior incus (L_I). The arrows illustrate the predicted relative magnitudes and directions of motion produced by sound pressure in the ear canal.

in our measurements), and localized displacement magnitudes that vary proportionally with the radial distance from the axis (Figs. 9A&B). This motion is consistent with the data of Figs. 5 & 6 at frequencies ≤ 2 kHz, which demonstrate a constancy in the relative phase, and graded displacement magnitudes that are largest at points furthest from the predicted axis. This consistency suggests that rotation around an AP axis dominates the sound-induced motion of the ossicles at frequencies below 2 kHz. Such AP axis rotation is consistent with low-frequency ossicular rotation described in humans by Dahmann (1929), Kirikae (1960) and Decraemer and Khanna (2004), in cat by Guinan and Peake (1967) and Decraemer and Khanna (2004), and in gerbil by Rosowski et al. (1999) and Decraemer et al. (2014).

4.3.2. Whole-body translation

At frequencies between 3 and 8 kHz, the data of Figs. 5 & 7 (and Supplemental Materials 3 through 8) continue to illustrate generally in-phase displacement of the ossicles, with an inferior-to-superior decrease in the magnitude of displacement. However, Fig. 5C and comparisons between Figs. 6 & 7 demonstrate the magnitudes of the manubrial displacements relative to the umbo are increased between 3 and 8 kHz compared to lower frequencies. This change is consistent with the addition of a translation mode of motion (Figs. 9C&D) acting together with the AP rotational mode, where the translation component is in phase with the AP-rotational component and has a magnitude of about 10% of the umbo displacement produced by AP rotation. The addition of this spatially 'constant' translational component to the AP rotational mode produces the small frequency-dependent step increase in the displacement magnitude along the manubrial arm between 3 and 8 kHz in Fig. 5C, where the effect of this spatially constant 'step' on the total displacement is larger at locations closer to the AP axis of rotation (e.g. the step with a magnitude of 0.1 in Fig. 5C, is most significant at the lateral process and decreases in influence closer to the umbo). The combination of lateral-medial translation and AP rotation was also identified in cat and human middle ears at frequencies above 1–2 kHz (Decraemer and Khanna 1994).

There is other evidence of whole-body translation in our displacement data. For example, the similar large displacement magnitude of much of the ossicular surfaces at 10.8 kHz in CHR3 (Fig. 7) suggests a significant translational component at that frequency in that ear. However, the continued lower magnitude motion of the lateral process at the superior-most part of the manubrium is not consistent with a simple summation of whole-body translation and AP rotation in a rigid system. Evidence for a large translational component of motion in the ear with the interrupted ISJ will be discussed in a later section.

4.3.3. IS-rotary axis

Fleischer (1978) was an early proponent of the presence of multiple axes of ossicular rotation whose relative influence on ossicular function varied with frequency. In his conception, rotation about the AP axis determined the motion of the ossicles at low frequencies, where the primary limits on ossicular motion were the stiffnesses of the ossicular support. In some species (e.g. mouse and rats), at frequencies above the low-frequency resonance where this stiffness was no longer significant, he suggested the onset of a second rotary mode of ossicular motion: rotation about an IS axis perpendicular to the AP axis and located between the incus and manubrial arms. Such a location would produce out-of-phase motion of the manubrium and the incus (Figs. 9E & 9F). The relative phase and magnitude of manubrial, incus and stapes displacements we present in Figs. 5B, 5D & 7 at frequencies between 10 and 18 kHz provide strong evidence for the presence of such rotations in the normal chinchilla ear. The primary indicator of this new rotation is that the motion of the incus and

stapes is nearly half a cycle out-of-phase relative to the motion of the umbo and manubrium. The half-cycle difference between the phase of motion of the rigidly-connected incus and malleus is especially strong support for this new mode of motion. In earlier conceptions of ossicular function, such inter-ossicular displacement phase and magnitude differences were often attributed to the action of the compliant incudomalleolar joint (Guinan and Peake 1967; Willi et al. 2002), which is absent in the chinchilla.

Others have investigated the existence of additional rotational modes in ossicular motion in other animals. Saunders and Summers (1982) measured the relative motion magnitudes of different points on the ossicular chain of mice using different sound frequencies. Their Fig. 5 demonstrates a frequency-dependent difference between the motion of the umbo and the body of the manubrium, where the motion of the malleal body decreases relative to the umbo with higher frequency sounds, as would be predicted by rotation about an IS axis. Though Saunders and Summers did not measure the relative phase of the displacements at these points, the measurements of Dong et al. (2013) reveal a half-cycle difference in the phase of motion between these two points on the mouse ossicular chain that develops between 20 and 50 kHz.

4.3.4. Bending of the ossicles

While we have first described three modes of rigid-body ossicular motion, the existence of coupled frequency-dependent differences in the phase of motion along the surface of the manubrium observed in Fig. 8 and reductions in the relative magnitude of motion at locations superior to the umbo in Figs. 5C and 7 at frequencies of 10 kHz and higher suggest the manubrium bends with higher frequencies of sound stimulation. Such bending could result from the distributed mass and stiffness along the manubrial arm that leads to reductions in transferred motion magnitude and increasing phase delays between the umbo and the lateral process. The phase angle data of Fig. 5C suggests such bending is most apparent above 8 kHz. The sudden decreases in relative motion magnitude at frequencies above 10 kHz in the same figure – that are graded along the manubrial arm with the largest decrease at the lateral process – is also consistent with bending along the manubrial arm. Bending of the manubrium is well-described in cat (Funnell et al. 1992; Decraemer et al. 1995).

We also see evidence of growing spatial phase-angle differences along the manubrium in the three intact ears illustrated in Fig. 8. With tonal stimuli between 7 and 16 kHz all three intact ears display transitions from 0 phase at the umbo to small negative phases (–0.05 to –0.15 cycles) at the lateral process. The spatial gradient of the negatively increasing phase, consistent with bending of the manubrium, is more prominent with stimuli near 11 kHz such that the motion of the most superior parts of the manubrium lag the umbo by as much as 0.15 cycles. Near 11 kHz, the phase gradient is not simply arranged along the inferior to superior direction, but includes an anterior-posterior tilt to the iso-phase contours along the manubrium that vary in direction and phase difference between the three ears. Anterior-posterior tilts of the iso-phase angle gradients are also seen between 15 and 18 kHz in Fig. 8. These tilted phase gradients are consistent with a rotation of the manubrium about an IS axis located within the manubrium, but could also represent a bending and twisting of the manubrium about its own long axis.

4.4. Chinchilla ossicular motion: Interrupted IS joint

The sound-induced motion measured in one ear with an interrupted incudostapedial joint (Fig 4B, 4C) demonstrated an increase in umbo and incus motion near 2 kHz as well as an increase in incus motion magnitude at frequencies above 10 kHz. A similar increase in the magnitude of motion of the TM and manubrium near

2 kHz have been observed in cat and guinea pig after interruption of the IS joint (Allen 1986; Peake et al. 1992; Zwislocki 1963); however, in chinchilla such an increase has only been describe at a significantly lower (0.25 kHz) frequency (Rosowski et al. 2006).

The interruption had little effect on the relative motions of the incus and malleus at frequencies less than 6 kHz (Fig. 6 & 7). In this frequency range the displacements along the manubrium are still in phase and the magnitude of motion decreases from the umbo to the lateral process, though it seems as if the umbo-relative motion at this most superior point on the malleus is slightly greater in magnitude after ISJ interruption. (The umbo-relative displacement magnitude in CH3 at the superior end of the manubrium with 5.2 kHz stimulation in Fig. 7 is about 0.25, while in CH4 with ISJ-interruption the umbo-relative displacement magnitude at the same frequency and a similar manubrial location is about 0.5.) Such a finding is consistent with a larger in-out translational component at 5.2 kHz in the ISJ interrupted ear. Fig. 7 points out even larger differences in displacement between the ears with intact and interrupted ISJ with sound stimuli above 10 kHz. At those higher frequencies we consistently see (i) a reduction in the magnitude variation along the manubrial arm after ISJ interruption (larger fractions of the manubrium move with a magnitude within 10–20% of the umbo), (ii) a sizeable increase in the umbo-relative magnitude of the lateral process (–0.8 in the ISJ interrupted ear at 15.9 and 17.8 kHz compared to ~0.3 with an intact ISJ), and (iii) in-phase motion of the incus and manubrium at frequencies between 10 and 18 kHz. These differences are consistent with an increase in the significance of the ossicular in-out translation and a decrease in the rotation about the IS axis. Such changes suggest that the presence of the stapes, including its constraining annular ligament and the high-impedance cochlear load, play a significant role in determining relative ossicular motions at frequencies above 10 kHz, such that the constraint of the stapes and cochlea appears to reduce in-out translation and encourage the presence of rotation about the IS axis.

An as yet undescribed mode of ossicular motion in the ISJ-interrupted ear is suggested by the higher-resolution phase maps of Fig. 8. In the bottom row of that figure, the phase of motion along the manubrium at 10.8 kHz shows an increasing phase lead from the inferior to superior regions of the manubrium. There are also suggestions of a smaller inferior to superior phase leads at higher frequencies. It may be that removal of the constraining annular ligament introduces another motion mode that leads to the reversal of the phase gradient along the manubrial arm.

4.5. Can the advent of a new rotational axis result in an increase in the transfer of sound through the middle ear?

The umbo-relative motion data we present in Figs. 5 and 7 (along with Supplemental Materials 3 through 8) point to the existence of an inferiorly-superiorly directed ossicular IS rotation axis in the chinchilla that dominates ossicular motion at frequencies between 10 and 18 kHz. Fleischer (1978) argued for the existence of a similar high-frequency dominant axis in small mammals, and Puria and Steele (2010) argued for a similar axis of rotation in humans functioning at frequencies above 6 kHz. Both of those reports further argued that frequencies where these new motion modes were significant were also associated with an increase in the sound-induced motion of the stapes. To investigate that possibility in the chinchilla we look for frequency-dependent changes in the relative motion of the ossicles, that were not dependent on other modes of ossicular motion.

We start by hypothesizing that Fig. 5C points out two dominant modes of motion in two different frequency ranges. As mentioned earlier, at frequencies below 2 kHz, the data of Fig. 5C are very well modeled by simple rotation around an AP-directed axis positioned

a short distance above the lateral process, with all the points on the manubrium moving in phase, and the umbo-relative magnitude of the motion half way up the manubrium having a value of 0.6, and the relative motion at the lateral process of 0.2. Between 2 and 8 kHz, the observed 10% increase in the umbo relative motion magnitude and continued in-phase behavior at all manubrial locations is well modeled by continued AP-rotation with the addition of a lateral-medial translational component with a magnitude equivalent to 10% of the umbo motion.

How the sum of AP-rotation and translation affect the sound-induced motion of the stapes and incus is less clear cut as Fig. 5D shows no clear step in the umbo-relative motion of the other two ossicles in the 2–8 kHz range. However, it is clear from Fig. 5C&D, and Figs. 6 and 7, that the motion of the stapes and incus at frequencies below 8 kHz is very similar to the motion of the manubrial location $\frac{3}{4}$ of the distance between the umbo and the lateral process. This similarity is quantified in Fig. 5E which plots the ratio of the displacement of the stapes footplate and the $\frac{3}{4}$ manubrial location in the individual ears and their average. At frequencies below 8 kHz the mean magnitude of the ratio falls between 0.85 and 1.3 and the mean phase angle varies between 0 and –0.03 cycles; these relatively small variations around a hypothesized relative magnitude of 1 and a relative phase of 0 support the notion of near equal motion of the stapes footplate and the $\frac{3}{4}$ manubrium position.

Between 8 and 15 kHz, in all three ears, the motion magnitude of the footplate grows relative to that of the $\frac{3}{4}$ position reaching a relative magnitude of between 2.5 and 4. In that same frequency range, the phase angle between the footplate and the $\frac{3}{4}$ manubrium position approaches –0.5 cycles. The concurrency of the phase change and magnitude increase suggests they both result from the onset of ossicular rotation about an IS axis positioned parallel to and near the manubrium, such that the lever-arm between the stapes footplate and the axis is 2 to 3 time larger than the lever-arm to the manubrium (Fig. 9E&F). Why the motion gain due to the addition of the new rotational mode cuts off above 17 kHz is not clear, but could be related to a high-frequency limitation in the new rotational mode and/or the introduction of other modes of ossicular motion.

4.6. The importance of the non-osseous ossicular supports in defining the modes of ossicular motion

Puria and Steele (2010) used micro-CT imaging of the isolated ossicles of human, cats, guinea pig and chinchilla to describe their shape and density. They then computed the first three principal moments of inertia and axes of rotations of the combined ossicles from these descriptions. The identified axis of rotation with the lowest moment of inertia described in chinchilla is consistent with the rotations about the AP axis that describe our observations of ossicular motion at frequencies below 2 kHz. However, neither of the other axes described by Puria and Steele (2010) are consistent with the IS axis rotations that we observed in the intact middle ear near 14 kHz. We suggest this inconsistency results from the influence of the ossicular supports and the load placed on the ossicular system by the asymmetrically placed cochlea and annular ligament that were not included in the Puria and Steele analyses. Our observation that rotations around the IS axis are reduced by removing the support of the annular ligament and the cochlear load are consistent with this view.

4.7. Implications for models of middle-ear function

Our and others' descriptions of multiple modes of ossicular motion (i) complicate circuit models that use anatomical and physical analogues to predict middle-ear function, (ii) describe new sources

for phase delay in middle-ear sound transmission, and (iii) provide new measurements for better testing of finite element models of the middle ear.

The implications of multiple motion modes on circuit models of the middle ear, which describe a single ossicular mode of motion in terms of anatomically and physically determined elements and element combinations, depend on the frequency range of middle-ear transmission that is modeled, and the accuracy required of the model. Circuit models of the chinchilla middle ear used to quantify middle-ear output at frequencies of 8 kHz that already account for AP axis rotation and ossicular bending will be little affected by our findings (e.g. Lemons & Meaud 2016; Bowers & Rosowski 2019). Accurate circuit models of function at frequencies above 10 kHz will require more complicated topography. For example, Hudde and Weistenhöfer (1997) describe a circuit model with multiple modes of motion, each described by separate model branches where the contributions of each branch to stapes motion is summed to compute the final output. Circuit models based on measurement-derived two-port analyses that do not require strict relationships between element values and anatomy or physics, and only assume the stapes undergoes in-and-out translation would already include the action of multiple motion modes within the matrix descriptions (e.g. Ravicz and Rosowski 2017), but could be in error when used to describe changes in middle-ear function under conditions that alter the balance of different motion modes, e.g., ISJ interruption.

The simplification that the middle ear acts as a transmission line is used commonly by those interested in high-frequency sound transmission (e.g. Olsen 1998; Puria and Allen 1998). Those authors argue that the phase-delay produced by the TM and the distributed masses and stiffness within the ossicular chain is well described by a fixed time delay that produces a constant phase gradient in the linear frequency domain. Such a phase change is not consistent with the half-cycle phase change we observe in a fairly narrow frequency range (10 to 18 kHz).

Finite element models should inherently include possible multiple modes of ossicular motion. Our data provides additional constraints on such models. Attempts at verification of these models should take our new observations into account.

5. Conclusion

We have scanned the middle ears of cadaveric chinchillas with a wavelength-swept OCT to describe the structure and sound-induced motion of the OCT visible surfaces of much of the ossicular chain at sound frequencies between 0.5 and 18 kHz. The displacements we measured are consistent with the presence of several different modes of motion, where each motion mode is best observed over a specific stimulus frequency range. Between 0.5 and 2 kHz the motion of the ossicles is consistent with rotation about an AP axis positioned near the anatomical axis defined by the anterior-malleal process and the posterior-incudal ligament. Between 2 and 8 kHz, the measured motion is consistent with the combination of anterior-posterior rotation and a lateral-medial translation. Between 8 and 18 kHz, our data suggest the presence of a dominant rotational mode defined by an IS directed axis that parallels and is positioned near the posterior edge of the manubrium of the malleus. This higher-order rotational mode is associated with a factor of 2 to 4 increase in the magnitude of stapes footplate displacement relative to the manubrium of the malleus and the introduction of a half-cycle step in the relative phase of stapes and umbo motion. Evidence of ossicular bending (Funnell et al. 1992; Decraemer & Khanna 1994; Decraemer et al. 1994) was also found in the graded magnitude and phase of motion along the manubrial surface, and was most

prominent above 10 kHz, where we observed significant reductions in the motion of the lateral process relative to the umbo.

Measurements in one ear with the incudostapedial joint (ISJ) interrupted did not exhibit rotations about the IS axis, but did show an increase in the relative size of the translational component of ossicular motion. These changes in modal motion after ISJ interruption point to the stapes, annular ligament and cochlea having a significant influence on the modes of ossicular motion. Perhaps the asymmetric placement of the stapes in the ossicular chain encourages the presence of IS rotations of ossicular motion, while the constraints of the stapes and cochlear load inhibit lateral-to-medial translation of the malleus and incus.

Many of these motions have been observed by others in cat, gerbil and human (e.g. Decraemer and Khanna 2004; Decraemer et al. 2014). However, our near simultaneous measurements of the sound-induced displacement of a large fraction of the chinchilla ossicular chain provide clear and simple evidence of such motions in an ear with a rigidly connected malleus and incus, and support the idea that frequency-dependent changes in the mode of ossicular motion contribute to the frequency dependence of the magnitude and phase of middle-ear sound transmission (Fleischer 1978; Puria and Steele 2010). Our results also point out that kinematic analyses of ossicular motion that ignore the effects of supporting ligaments and other ossicular supports and constraints (e.g. Puria and Steele 2010; Péus et al. 2020) can lead to inaccurate predictions of modes of ossicular motion.

Author statement

Professors Rosowski and Cheng were primarily responsible for planning the work, preparing the animal specimens, and designing and implementing the acoustical stimulus and measurement systems.

Professor Yun and Dr. Ramier designed and implemented the OCT system and integrated the optical and acoustic measurements.

All experiments were performed by Rosowski, Cheng and Ramier together.

Data analysis was performed by Drs. Ramier and Rosowski.

The writing was performed by Dr. Rosowski with significant input from and editing by the other three authors.

Acknowledgments

We wish to thank Dr. James Kobler of the Department of Surgery at Harvard Medical School and the Massachusetts General Hospital, who initiated the collaboration between the Rosowski and Yun research groups. Dr. Peter Bowers contributed to the discussions and was responsible for gathering the microCT data (performed at the Center for Skeletal Research at Massachusetts General Hospital, Boston MA UAS) used in Fig. 9. Mike Ravicz contributed to the discussions of this work and to the design and manufacture of the acoustic measurement equipment. Two anonymous reviewers contributed greatly to the final manuscript. The work was funded by the US National Institutes for Health: R01DC00194 and P41-EB015903, and Fonds de Recherche du Québec.

Supplementary materials

Supplementary material associated with this article can be found, in the online version, at doi:10.1016/j.heares.2020.108056.

References

- Allen, J.B., 1986. Measurements of eardrum acoustic impedance. In: Allen, J., Hall, J., Hubbard, A., Neely, S., Tubis, A. (Eds.), *Peripheral Auditory Mechanisms*. Springer-Verlag, New York, pp. 44–51 pg.

- Ball, GR, Huber, A, Goode, RL, 1997. Scanning laser Doppler vibrometry of the middle ear ossicles. *Ear Nose Throat J.* 76, 213–218.
- von Békésy, G, 1960. *Experiments in Hearing*. McGraw-Hill, New York.
- Blayney, AW, Williams, KR, Rice, HJ, 1997. A dynamic and harmonic damped finite element analysis model of stapedotomy. *Acta Otolaryngol.* 117, 269–273.
- Bowers, PN., 2020. *Characterization of Bone-Conduction Mechanisms in Chinchilla Using In Vivo Measurements and Impedance Models*. PhD. Harvard University.
- Bowers, PN, Rosowski, JJ., 2019. A lumped-element model of the chinchilla ear. *J. Acoust. Soc. Am.* 145, 1975–1992.
- Burkhardt, A, Kirsten, L, Bornitz, M, Zahnert, T, Koch, E, 2014. Investigation of the human tympanic membrane oscillation ex vivo by Doppler optical coherence tomography. *J. Biophotonics* 7, 434–441.
- Chang, EW, Cheng, JT, Rööslö, C, Kobler, JB, Rosowski, JJ, Yun, SH, 2013. Simultaneous 3D imaging of sound-induced motions of the tympanic membrane and middle ear ossicles. *Hear. Res.* 304, 49–56.
- Cheng, JT, Hamada, M, Harrington, E, Furlong, C, Merchant, SN, Rosowski, JJ, 2013. Wave motion on the surface of the human tympanic membrane: holographic measurement and modeling analysis. *J. Acoust. Soc. Am.* 133, 918–937.
- Dahmann, H., 1929. Zur Physiologie des Hörens; experimentelle Untersuchungen über die Mechanik der Gehörknöchelchenkette sowie über deren Verbalten auf Ton und Luftdruck: I. *Zeits f Hals-Nasen-Ohrenheilk* 24, 462–467.
- Decraemer, WF, de La Rochefoucauld, O, Funnell, WRJ, Olson, ES, 2014. Three-dimensional vibration of the malleus and incus in the living gerbil. *J. Assoc. Res. Otolaryngol.* 15, 483–510.
- Decraemer, W, Khanna, SM., 1994. Modelling the malleus vibration as a rigid body motion with one rotational and one translational degree of freedom. *Hear. Res.* 72, 1–18.
- Decraemer, WF, Khanna, SM., 2004. Measurement, visualization and quantitative analysis of complete three-dimensional kinematical data sets of human and cat middle ear. In: Gyo, K, Wada, H, Hato, N, Koike, T (Eds.), *Middle Ear Mechanics in Research and Otology*. World Scientific, Singapore, pp. 3–10.
- Decraemer, WF, Khanna, SM, Funnell, WRJ, 1991. Malleus vibration mode changes with frequency. *Hear. Res.* 54, 305–318.
- Decraemer, WF, Khanna, SM, Funnell, WRJ, 1994. A method for determining three-dimensional vibration in the ear. *Hearing Res.* 77, 19–37.
- Decraemer, WF, Khanna, SM, Funnell, WRJ, 1995. Bending of the manubrium in cat under normal sound stimulation. *Prog. Biomed. Opt.* 2329, 74–84.
- Decraemer, WF, Khanna, SM, Funnell, WRJ, 1997. Vibrations of the cat tympanic membrane measured with high spatial resolution. In: *Proceedings of the 20th Midwinter Meeting of the Association for Research in Otolaryngology*, Abstract 192.
- De Greef, D, Buytaert, JAN, Aerts, JRM, Van Hoorebeke, L, Dierick, M, Dirckx, J, 2015. Details of human middle ear morphology based on micro-CT imaging of phosphotungstic acid stained samples. *J. Morphol.* 276, 1025–1046.
- de La Rochefoucauld, O, Khanna, SM, Olson, ES, 2005. Recording depth and signal coherence in heterodyne interferometry. *J. Acoust. Soc. Am.* 117, 1267–1284.
- de La Rochefoucauld, O, Decraemer, WF, Khanna, SM, Olson, ES, 2008. Simultaneous measurements of ossicular velocity and intracochlear pressure leading to the cochlear input impedance in Gerbil. *J. Assoc. Res. Otolaryngol.* 9, 161–177.
- Djalilian, HR, Rubinstein, M, Wu, EC, Naemi, K, Zardouz, S, Karimi, K, Wong, BJ, 2010. Optical coherence tomography of cholesteatoma. *Otol. Neurotol.* 31, 932–935.
- Dong, W, Varavva, P, Olson, ES, 2013. Sound transmission along the ossicular chain in common wild-type laboratory mice. *Hear. Res.* 301, 27–34.
- Fleischer, G., 1978. Evolutionary principles of the mammalian middle ear. *Adv. Anat. Embryol. Cell Biol.* 55, 3–69.
- Funnell, WR, Khanna, SM, Decraemer, WF, 1992. On the degree of rigidity of the manubrium in a finite-element model of the cat eardrum. *J. Acoust. Soc. Am.* 91, 2082–2090.
- Gan, RZ, Feng, B, Sun, Q, 2004. Three-dimensional finite element modeling of human ear for sound transmission. *Ann. Biomed. Eng.* 32, 847–859.
- Guinan Jr, JJ, Peake, WT, 1967. Middle-ear characteristics of anesthetized cats. *J. Acoust. Soc. Am.* 41, 1237–1261.
- Hemilä, S, Nummela, S, Reuter, T, 1995. What middle ear parameters tell about impedance matching and high frequency hearing. *Hear. Res.* 85, 31–44.
- Hudde, H, Weistenhöfer, C., 1997. A three-dimensional circuit model of the middle ear. *Acustica (Acta Acustica)* 83, 535–549.
- Kirikae, I, 1960. *The Structure and Function of the Middle Ear*. University of Tokyo Press, Tokyo.
- Koike, T, Wada, H, Kobayashi, T, 2002. Modeling of the human middle ear using the finite-element method. *J. Acoust. Soc. Am.* 111, 1306–1317.
- Kringlebotn, M., 1988. Network model for the human middle ear. *Scand. Audiol.* 17, 75–85.
- Ladak, J, Funnell, WRJ., 1996. Finite-element modeling of the normal and surgically repaired cat middle ear. *J. Acoust. Soc. Am.* 100, 933–944.
- Lauxmann, M, Eiber, A, Heckeler, C, Irlir, S, Chatzimichalis, M, Huber, A, Sim, JH, 2012. In-plane motions of the stapes in human ears. *J. Acoust. Soc. Am.* 132, 3280–3291.
- Lemons, C, Meaud, J., 2016. Middle-ear function in the chinchilla: circuit models and comparison with other species. *J. Acoust. Soc. Am.* 140, 2735–2753.
- MacDougall, D, Farrell, J, Brown, J, Bance, M, Adamson, R, 2016. Long-range, wide-field swept-source optical coherence tomography with GPU accelerated digital lock-in Doppler vibrometry for real-time, in vivo middle ear diagnostics. *Biomed. Opt. Express* 7, 4621.
- Manley, GA, Johnstone, BM., 1974. Middle-ear function in the guinea pig. *J. Acoust. Soc. Am.* 56, 571–576.
- Møller, AR., 1963. Transfer function of the middle ear. *J. Acoust. Soc. Am.* 35, 1526–1534.
- Nakajima, HH, Dong, W, Olson, ES, Merchant, SN, Ravicz, ME, Rosowski, JJ, 2009. Differential intracochlear sound pressure measurements in normal human temporal bones. *J. Assoc. Res. Otolaryngol.* 10, 23–36.
- O'Connor, KN, Cai, H, Puria, S, 2017. The effects of varying tympanic-membrane material properties on human middle-ear sound transmission in a three-dimensional finite-element model. *J. Acoust. Soc. Am.* 142, 2836–2853.
- Olson, ES., 1998. Observing middle and inner ear mechanics with novel intracochlear pressure sensors. *J. Acoust. Soc. Am.* 103, 3445–3463.
- Park, J, Carbajal, EF, Chen, X, Oghalai, JS, Applegate, BE, 2014. Phase-sensitive optical coherence tomography using a Vernier-tuned distributed Bragg reflector swept laser in the mouse middle ear. *Opt. Lett.* 39, 6233–6236.
- Park, J, Cheng, JT, Ferguson, D, Maguluri, G, Chang, EW, Clancy, C, Lee, DJ, Iftimia, N, 2016. Investigation of middle ear anatomy and function with combine video otoscopy-phase sensitive OCT. *Biomed. Opt. Exp.* 7, 252253.
- Peake, WT, Rosowski, JJ, Lynch III, TJ, 1992. Middle-ear transmission: acoustic vs. ossicular coupling in cat and human. *Hear. Res.* 57, 245–268.
- Péus, D, Dobrev, I, Pffiffer, F, Sim, JH, 2020. Comparison of sheep and human middle-ear ossicles: anatomy and inertial properties. *J. Comput. Physiol. A Neuroethol. Sens. Neural Behav. Physiol.* doi:10.1007/s00359-020-01430-w, on line at.
- Pitris, C, Saunders, KT, Fujimoto, JG, Brezinski, ME, 2001. High-resolution imaging of the middle ear with optical coherence tomography: a feasibility study. *Arch. Otolaryngol. Head Neck Surg.* 127, 637–642.
- Puria, S, Allen, JB., 1998. Measurements and model of the cat middle ear: evidence of tympanic membrane acoustic delay. *J. Acoust. Soc. Am.* 104, 3463–3481.
- Puria, S, Steele, C., 2010. Tympanic-membrane and malleus-incus-complex co-adaptations for high-frequency hearing in mammals. *Hear. Res.* 263, 183–190.
- Ramier, A, Cheng, JT, Ravicz, ME, Rosowski, JJ, Yun, SH, 2018a. Mapping the phase and amplitude of ossicular chain motion using sound-synchronous optical coherence vibrometry. *Bio Opt. Express* 9, 5489.
- Ramier, A, Puria, S, Rosowski, JJ, Yun, SH, 2018b. Optical coherence tomography for imaging the middle and inner ears: a technical review. *Mech. Hear.* 2017 C Bergevin, S Puria, CA Spera.
- Ravicz, ME, Rosowski, JJ., 2013. Middle-ear velocity transfer function, cochlear input immittance and middle-ear efficiency in chinchilla. *J. Acoust. Soc. Am.* 134, 2852–2865.
- Ravicz, ME, Rosowski, JJ., 2017. Chinchilla middle-ear transmission matrix representation, revisited. *J. Acoust. Soc. Am.* 141, 3274–3290.
- Robles, L, Temchin, AN, Fan, Y-H, Ruggero, MA, 2015. Stapes vibration in the chinchilla middle ear: relation to behavioral and auditory-nerve thresholds. *J. Assoc. Res. Otolaryngol.* 16, 447–457.
- Rosowski, JJ, Cheng, JT, Ravicz, ME, Hulli, N, Harrington, EJ, Hernandez-Montes, MS, Furlong, C, 2009. Computer-assisted time-averaged holography of the motion of the surface of the tympanic membrane with sound stimuli of 0.4 to 25 kHz. *Hear. Res.* 253, 83–96.
- Rosowski, JJ, Ravicz, ME, Songer, JE, 2006. Structures that contribute to middle-ear admittance in chinchilla. *J. Comp Physiol A* 192, 1287–1311.
- Rosowski, JJ, Ravicz, ME, Teoh, SW, Flandermeyer, D, 1999. Measurements of Middle-Ear Function in the Mongolian Gerbil, a Specialized Mammalian Ear. *Audiol. Neurotol.* 4, 129–136.
- Ruggero, MA, Rich, NC, Robles, L, Shivapuja, BG, 1990. Middle ear response in the chinchilla and its relationship to mechanics at the base of the cochlea. *J. Acoust. Soc. Am.* 87, 1612–1629.
- Ruggero, MA, Temchin, AN., 2002. The roles of the external, middle and inner ears in determining the bandwidth of hearing. *Proc. Natl. Acad. Sci.* 99, 13206–13210.
- Saunders, JC, Summers, RM., 1982. Auditory structure and function in the mouse middle ear: an evaluation by SEM and capacitive probe. *J. Comput. Physiol. A* 146, 517–525.
- Subhash, HM, Nguyen-Huynh, A, Wang, RK, Jacques, SL, Choudhury, N, Nuttall, AL, 2012. Feasibility of spectral-domain phase-sensitive optical coherence tomography for middle ear vibrometry. *J. Biomed. Opt.* 17, 060505.
- Sim, JH, Puria, S., 2008. Soft tissue morphometry of the malleus-incus complex from micro-CT imaging. *J. Assoc. Res. Otolaryngol.* 9, 5–21.
- Vrettakos, PA, Dear, SP, Saunders, JC, 1988. Middle-ear structure in the chinchilla: a quantitative study. *Am. J. Otolaryngol.* 9, 58–67.
- Wang, X, Gan, RZ., 2018. Surface motion of tympanic membrane in a chinchilla model of acute otitis media. *J. Assoc. Res. Otolaryngol.* 19, 619–635.
- Wang, X, Gan, RZ., 2016. 3D finite element model of the chinchilla ear for characterizing middle ear functions. *Biomed. Model. Mechanobiol.* 15, 1263–1277.
- Wever, EG, Lawrence, M., 1954. *Physiological Acoustics*. Princeton University Press, Princeton.
- Willi, UB, Ferrazzini, MA, Huber, AM, 2002. The incudo-malleolar joint and sound transmission loss. *Hear. Res.* 174, 32–44.
- Zwislocki, J., 1962. Analysis of the middle-ear function. Part I: input impedance. *J. Acoust. Soc. Am.* 34, 1514–1523.
- Zwislocki, J., 1963. Analysis of the middle ear function. Part II. Guinea-pig ear. *J. Acoust. Soc. Am.* 35, 1034–1040.